



**HAL**  
open science

## **Rapid Response Mode observations of GRB 160203A: Looking for fine-structure line variability at $z=3.52$**

G Pugliese, A Saccardi, V.D Elia, S.D Vergani, K.E Heintz, S Savaglio, L Kaper, A de Ugarte Postigo, D.H Hartmann, A de Cia, et al.

► **To cite this version:**

G Pugliese, A Saccardi, V.D Elia, S.D Vergani, K.E Heintz, et al.. Rapid Response Mode observations of GRB 160203A: Looking for fine-structure line variability at  $z=3.52$ . *Astron.Astrophys.*, 2024, 690, pp.A35. 10.1051/0004-6361/202244098 . hal-04645120

**HAL Id: hal-04645120**

**<https://hal.science/hal-04645120v1>**

Submitted on 17 Jan 2025















**HAL** is a multi-disciplinary open access archive for the deposit and dissemination of scientific research documents, whether they are published or not. The documents may come from teaching and research institutions in France or abroad, or from public or private research centers.

L'archive ouverte pluridisciplinaire **HAL**, est destinée au dépôt et à la diffusion de documents scientifiques de niveau recherche, publiés ou non, émanant des établissements d'enseignement et de recherche français ou étrangers, des laboratoires publics ou privés.



Distributed under a Creative Commons Attribution 4.0 International License

# Rapid Response Mode observations of GRB 160203A: Looking for fine-structure line variability at $z = 3.52$

G. Pugliese<sup>1</sup> <sup>\*</sup>, A. Saccardi<sup>2</sup> , V. D'Elia<sup>3,4</sup>, S. D. Vergani<sup>2,5,6</sup>, K. E. Heintz<sup>7,8</sup>, S. Savaglio<sup>9,10,11</sup> , L. Kaper<sup>1</sup> , A. de Ugarte Postigo<sup>12</sup> , D. H. Hartmann<sup>13</sup> , A. De Cia<sup>14</sup>, S. Vejlgaard<sup>7,8</sup> , J. P. U. Fynbo<sup>7,8</sup> , L. Christensen<sup>7,8</sup> , S. Campana<sup>6</sup> , D. van Rest<sup>1</sup>, J. Selsing<sup>7,8</sup>, K. Wiersema<sup>15</sup>, D. B. Malesani<sup>7,8,16</sup>, S. Covino<sup>10</sup> , D. Burgarella<sup>14</sup>, M. De Pasquale<sup>17</sup>, P. Jakobsson<sup>8</sup> , J. Japelj<sup>1</sup>, D. A. Kann<sup>18,†</sup>, C. Kouveliotou<sup>19,20</sup> , A. Rossi<sup>10</sup>, N. R. Tanvir<sup>21</sup>, C. C. Thöne<sup>22</sup> , and D. Xu<sup>23</sup>

<sup>1</sup> Astronomical Institute Anton Pannekoek, University of Amsterdam, 1090 GE Amsterdam, The Netherlands

<sup>2</sup> GEPI, Observatoire de Paris, Université PSL, CNRS, 5 place Jule Janssen, 92190 Meudon, France

<sup>3</sup> Space Science Data Center (SSDC) – Agenzia Spaziale Italiana (ASI), 00133 Roma, Italy

<sup>4</sup> INAF – Osservatorio Astronomico di Roma, Via Frascati 33, 00040 Monte Porzio Catone, Italy

<sup>5</sup> Institut d'Astrophysique de Paris, UMR 7095, CNRS-SU, 98 bis boulevard Arago, 75014 Paris, France

<sup>6</sup> INAF – Osservatorio Astronomico di Brera, Via E. Bianchi 46, 23807 Merate (LC), Italy

<sup>7</sup> Cosmic Dawn Center (DAWN), Rådmandsgade 64, 2200 København N, Denmark

<sup>8</sup> Niels Bohr Institute, University of Copenhagen, Jagtvej 128, 2200 Copenhagen N, Denmark

<sup>9</sup> Department of physics, University of Calabria, Via P. Bucci, Arcavacata di Rende (CS), Italy

<sup>10</sup> INAF – Osservatorio di Astrofisica e Scienza dello Spazio, Via Piero Gobetti 93/3, 40129 Bologna, Italy

<sup>11</sup> INFN – Laboratori Nazionali di Frascati, Frascati, Italy

<sup>12</sup> Artemis, Observatoire de la Côte d'Azur, Université Côte d'Azur, CNRS, 06304 Nice, France

<sup>13</sup> Department of Physics & Astronomy, Clemson University, Clemson, SC 29634, USA

<sup>14</sup> European Southern Observatory, Karl-Schwarzschild Str. 2, 85748 Garching bei München, Germany

<sup>15</sup> Physics Department, Lancaster University, Lancaster, LA1 4YB, UK

<sup>16</sup> Department of Astrophysics/IMAPP, Radboud University, 6525 AJ Nijmegen, The Netherlands

<sup>17</sup> University of Messina, Department of Mathematics, Informatics, Physics and Earth Sciences, Polo Papardo, Via Stagno d'Alcontres 31, 98166 Messina, Italy

<sup>18</sup> Hessian Research Cluster ELEMENTS, Giersch Science Center, Max-von-Laue-Strasse 12, Goethe University Frankfurt, Campus Riedberg, 60438 Frankfurt am Main, Germany

<sup>19</sup> Physics Department, George Washington University, 725 21st Street NW, Washington, DC 20052, USA

<sup>20</sup> Astronomy, Physics, and Statistics Institute of Sciences (APSIS), George Washington University, Washington, DC 20052, USA

<sup>21</sup> Department of Physics and Astronomy, University of Leicester, University Road, Leicester LE1 7RH, UK

<sup>22</sup> Astronomical Institute, Czech Academy of Sciences, Fričova 298, Ondřejov, Czech Republic

<sup>23</sup> Key Laboratory of Space Astronomy, National Astronomical Observatories, Chinese Sciences Academy, Beijing 100101, China

Received 23 May 2022 / Accepted 24 June 2024

## ABSTRACT

**Context.** Gamma-ray bursts are the most energetic known explosions. Although they fade rapidly, they give us the opportunity to measure redshift and important properties of their host galaxies. We report the photometric and spectroscopic study of the *Swift* GRB 160203A at  $z = 3.518$ , and its host galaxy. Fine-structure absorption lines, detected in the afterglow at different epochs, allow us to investigate variability due to the strong fading background source.

**Aims.** We obtained two optical to near-infrared spectra of the GRB afterglow with X-shooter on ESO/VLT, 18 minutes and 5.7 hours after the burst, allowing us to investigate temporal changes of fine-structure absorption lines.

**Methods.** We measured H I column density  $\log N(\text{H I}/\text{cm}^{-2}) = 21.75 \pm 0.10$ , and several heavy-element ions along the GRB sightline in the host galaxy, among which Si II, Al II, Al III, C II, Ni II, Si IV, C IV, Zn II and Fe II, and Fe II\* and Si II\* fine-structure transitions from energetic levels excited by the afterglow, at the common redshift  $z = 3.518$ . We measured  $[\text{M}/\text{H}]_{\text{TOT}} = -0.78 \pm 0.13$  and a  $[\text{Zn}/\text{Fe}]_{\text{FT}} = 0.69 \pm 0.15$ , representing the total (dust corrected) metallicity and dust depletion, respectively. We detected additional intervening systems along the line of sight at  $z = 1.03$ ,  $z = 1.26$ ,  $z = 1.98$ ,  $z = 1.99$ ,  $z = 2.20$ , and  $z = 2.83$ . We could not measure significant variability in the strength of the fine-structure lines throughout all the observations and determined an upper limit for the GRB distance from the absorber of  $d < 300$  pc, adopting the canonical UV pumping scenario. However, we note that the quality of our data is not sufficient to conclusively rule out collisions as an alternative mechanism.

**Results.** GRB 160203A belongs to a growing sample of GRBs with medium resolution spectroscopy, provided by the *Swift*/X-shooter legacy programme, which enables a detailed investigation of the interstellar medium in high-redshift GRB host galaxies. In particular, this host galaxy shows relatively high metal enrichment and dust depletion already in place when the universe was only 1.8 Gyr old.

**Key words.** techniques: spectroscopic – galaxies: abundances – galaxies: ISM – gamma-ray burst: individual: grb 160203a

\*Corresponding author; [pugliese@astroduo.org](mailto:pugliese@astroduo.org)

† Deceased.

## 1. Introduction

Long Gamma-ray bursts (GRBs) (with prompt  $\gamma$ -ray emission duration  $> 2$  s) have been predominantly shown to be associated with the final stages of the lives of massive stars (Bégué & Pe'er 2015; Gehrels & Razzaque 2013; Piranomonte et al. 2015; Cano et al. 2017). While it is true that some GRBs with  $T_{90} > 2$  s have recently been shown to be the result of compact binary mergers (Rastinejad et al. 2022; Levan et al. 2024), they are very unlikely to contaminate high-redshift samples, due to the typically fainter luminosities of merger-driven GRBs and longer lifetimes of their progenitors following star formation. Thanks to their high luminosities, they have been detected up to very high redshifts ( $z \gtrsim 8$ , Salvaterra et al. 2009; Tanvir et al. 2009; Cucchiara et al. 2011; Tanvir et al. 2018), and are used to measure the metal enrichment of high- $z$  galaxies, thereby probing the chemical-enrichment history of the universe starting from the epoch of reionisation (Fynbo et al. 2006; Campana et al. 2007; Prochaska et al. 2008; Elliott et al. 2012; Tanvir et al. 2012; Hartoog et al. 2013; Saccardi et al. 2023).

During the last 14 years programmes such as the VLT/X-shooter GRB consortium and more recently the Stargate collaboration (Selsing et al. 2019) have provided detailed studies of the chemical composition and molecular gas in the interstellar medium of high-redshift galaxies (Salvaterra et al. 2012; Thöne et al. 2013; D’Elia et al. 2014; Hartoog et al. 2015; Krühler et al. 2015; Heintz et al. 2018; Zafar et al. 2018; Bolmer et al. 2019).

The X-shooter GTO programme first and the Stargate Consortium afterwards used the medium-resolution (resolving power  $\sim 8000$ ) VLT/X-shooter optical–near-IR (NIR) spectrograph and have provided to date a sample of more than 120 GRB afterglows (Selsing et al. 2019), including 22 GRB afterglows with metallicity measurements (Bolmer et al. 2019). They also have largely contributed to our knowledge of the chemical properties of high- $z$  galaxies, both with sample studies (Christensen et al. 2017; Wiseman et al. 2017; Heintz et al. 2019; Tanvir et al. 2019), and with detailed studies on individual GRBs (Sparre et al. 2014; de Ugarte Postigo et al. 2018; Saccardi et al. 2023). However, the number of observed GRB host galaxies for which the metal abundance has been determined is still relatively small (about 49 GRBs), and is usually limited by spectral resolution and low signal-to-noise ratio (S/N; Krühler et al. 2015; Cucchiara et al. 2015).

The need for a larger sample has been addressed in multiple studies (Nagamine et al. 2008; Cucchiara et al. 2016), where it was emphasised how the long-duration GRB peculiarity of probing mainly the inner active regions of their host galaxies can be an independent way to investigate the chemical composition of high-redshift galaxies (Savaglio et al. 2003; Prochaska et al. 2009; Tanvir et al. 2018; Palmerio et al. 2019). In addition, relative abundances of metals with different refractory properties are indicative of conditions in the local GRB environment (see De Cia 2018 for an overview).

In addition, GRB afterglow spectra have also shown that these huge photon sources can generate a UV pumping mechanism revealed by the variability of fine-structure lines (Vreeswijk et al. 2007; D’Elia et al. 2011). The variability has been used to reconstruct the effects of GRBs and afterglow radiation on the absorbing regions, demonstrating that they can influence their surrounding typically up to a few hundred parsec (Ledoux et al. 2009; D’Elia et al. 2009; De Cia et al. 2012; Thöne et al. 2013; Vreeswijk et al. 2013; Schady 2015; de Ugarte Postigo et al. 2018). This in turn allows the distance between the GRB and

the absorbing material to be measured, providing a 3D view of the medium in the GRB host galaxies.

Despite the unique insight of high-redshift star-forming regions provided by fine-structure line variation studies, the number of GRBs having suitable data for this purpose is still very limited (D’Elia et al. 2010; Krühler et al. 2013; D’Elia et al. 2014; Wiseman et al. 2017; Tanvir et al. 2018; Zafar et al. 2018), due to the need to obtain time series of spectra, starting as soon as possible after the GRB trigger. Rapid Response Mode (RRM) observations were developed at VLT also driven by this specific science case. In this mode, the telescope is robotically triggered, and observations are commenced rapidly (within minutes) after a GRB, a unique feature among large-aperture telescopes. However, the unfortunate location of the VLT with respect to the South Atlantic Anomaly (which limits the number of GRB triggers from *Swift* immediately observable from Paranal), coupled with the availability of the telescope and instruments, make successful RRM observations very rare. Therefore, any new observational RRM campaign of high-redshift GRBs, focusing on the variability of fine-structure lines, contributes significantly to our knowledge of active star-forming regions in the young Universe.

As a part of the VLT/X-shooter GRB follow-up programme, here we report the spectra of the afterglow of GRB 160203A at a redshift of  $z = 3.518$ , at two different epochs, 18 minutes after the  $\gamma$ -ray detection and 5.7 hours after the first detection. This was the first GRB detected with the *Neil Gehrels Swift* Observatory (*Swift* hereafter) observed by X-shooter in RRM.

In Section 2 we discuss the main features and reduction of our VLT/X-shooter data. In Section 3 we present the results of our analysis of the property of the host galaxy, and the chemical abundances and metallicities. In Section 4 we report our results on the variability of the fine-structure lines. In Section 5 we discuss the interaction between the GRB and its environment, and in Section 6 we summarise the main outcomes of our study, also comparing them with previous analyses.

We used the following cosmological parameters:  $H_0 = 71$  km s $^{-1}$ Mpc $^{-1}$ ,  $\Omega_M = 0.27$ , and  $\Omega_\Lambda = 0.73$ . Time is assumed to be in the observer frame. Unless otherwise stated, throughout the paper the uncertainties are  $1\sigma$  and the limits are  $3\sigma$ .

## 2. GRB 160203A: Observations

### 2.1. *Swift* observations

GRB 160203A was a long event with a duration (i.e. the time in which 90% of the counts of the prompt  $\gamma$ -ray emission are detected)  $T_{90} = 20.2$ . It was detected by the Burst Alert Telescope (BAT) instrument on board *Swift* (Gehrels et al. 2004) at 02:13:10 UT on 3 February 2016 (hereafter considered as  $T_0$ ; D’Avanzo et al. 2016).

The BAT light curve was characterised by a prominent central peak at  $T_0 + 12$  s, preceded and followed by less intense activity, and a spectral photon index in the gamma-ray band equal to  $1.93 \pm 0.20$ . The initial observed flux recorded by the *Swift* X-Ray Telescope (XRT) in the (0.3–10) keV energy band was  $1.55^{+0.23}_{-0.20} \times 10^{-12}$  erg cm $^{-2}$  s $^{-1}$ . The energy spectrum can be described by a single power law with a photon index of  $1.76^{+0.23}_{-0.16}$  in the same energy band, absorbed by a rest-frame hydrogen-equivalent column density  $N_H = 1.5^{+2.6}_{-1.5} \times 10^{22}$  cm $^{-2}$  (Osborne et al. 2016).

Assuming a broken power law temporal decay,  $F(t) \propto t^{-\alpha}$  for the (0.3–10) keV flux, the *Swift* collaboration also reported an

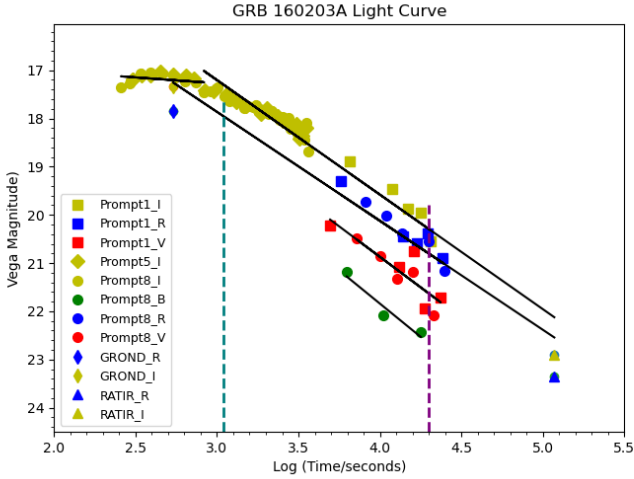


**Fig. 1.** Optical light curve of GRB 160203A with data taken by the Skynet telescopes 16'' telescope (all Prompt5 array data) and two 24'' telescopes (all Prompt1 and Prompt8 array data) at Cerro Tololo Inter-American Observatory (CTIO), Chile. GROND and RATIR photometric data are also included. The dashed green line corresponds to the time of our RRM observation (Epoch 1), while the dashed purple line corresponds to the second epoch of observation (Epoch 2), both performed with X-shooter on the VLT. The black lines are the best fit for each observed band.

initial decay in the XRT light curve with a slope  $\alpha_1 = 3.1^{+1.0}_{-0.9}$ , and a first break at  $246^{+773}_{-47}$  seconds after the  $\gamma$ -ray detection. A subsequent decay with a slope  $\alpha_2 = 0.65^{+0.11}_{-1.97}$  was followed by another break in the light curve recorded at  $6808^{+4410}_{-6181}$  seconds after the  $\gamma$ -ray detection. The third and final decay phase is characterised by a slope of  $\alpha_3 = 1.25^{+0.22}_{-0.16}$  (Evans et al. 2009). No *Swift*/UVOT detection was reported with a magnitude limit  $U > 19.5$  (Breeveld & D’Avanzo 2016).

## 2.2. Optical-NIR Photometry

The first reported ground-based observations in the optical–NIR band of GRB 160203A were carried out with GROND (Greiner et al. 2008) operating at the 2.2m MPG telescope at ESO La Silla observatory in Chile, about six minutes after the  $\gamma$ -ray detection, identifying an unknown source at the position RA(J2000.0) = 10:47:48.35, Dec(J2000.0) = –24:47:19.8 with a preliminary magnitude in the AB system  $r' = 18.0 \pm 0.1$  (Kruehler et al. 2016).

Simultaneously with the GROND detection of the optical afterglow, the Skynet collaboration (Trotter et al. 2016) obtained a more extensive ground-based follow-up of GRB 160203A, using their set of automated optical telescopes with apertures between 14 and 40 inches in diameter. The Skynet observations were used to create the optical light curve shown in Fig. 1. The data points were computed in the Vega magnitude systems.

A later follow-up was reported by Butler et al. (2016), using the Reionization And Transients Infra-Red (RATIR) camera on the Harold Johnson Telescope about 32.6 hours after the  $\gamma$ -ray detection by *Swift*. We converted their magnitude (reported in the AB system) to the Vega system (Fig. 1).

We performed photometry of the acquisition images obtained with X-shooter as part of the target acquisition procedure immediately prior to the spectroscopic observations (see Fig. 2). These images were obtained in the *R* filter, and consisted of two frames of 15 seconds and 5 seconds exposure time,

respectively. The afterglow was observed to fade by  $2.38 \pm 0.07$  magnitudes between the first and second epoch, as compared to five field stars, in agreement with the photometry collected in Fig. 1. We also performed fits to all magnitudes reported publicly in GCN circulars (Fig. 1), using a smoothly broken power law, and obtained indices  $0.03^{+0.13}_{-0.09}$  and  $1.30^{+1.36}_{-1.24}$  at 90% confidence, which agrees with the X-shooter acquisition data value. There was no evidence of a jet break in the light curve of the afterglow of GRB 160203A.

## 2.3. Spectroscopic observations and data reduction

Optical and near-infrared spectra of GRB 160203A were obtained in RRM with X-shooter (first reported in Pugliese et al. 2016) starting on 3 February 02:31:35 UT, just 18 minutes after the  $\gamma$ -ray alert (Table 1). This was not the first time that our collaboration obtained a GRB spectrum using RRM, but this was the first time in which we succeeded to perform a second set of observations, about 5.7 hours after the alert, again using the X-shooter instrument (Table 1).

For clarity, we refer to all the observations taken in RRM as Epoch 1 and to the observations taken 5.7 hours after the first BAT trigger as Epoch 2.

The three X-shooter arms cover the UVB (3000–5600 Å), visible (5500–10200 Å), and NIR (10200–24 800 Å) bands simultaneously (Vernet et al. 2011). The observation was obtained with a slit width of 1.0, 0.9, and 0.9 arcsec in the UVB, VIS, and NIR arms, respectively, and a nominal resolving power  $R = \lambda/\Delta\lambda$  of  $R = 5400$ ,  $R = 8900$ , and  $R = 5600$ . These  $R$  values correspond to a velocity resolution of about 56, 34, and 54 km s<sup>–1</sup> in the UVB, VIS, and NIR arms, respectively. The velocity structure is typically used as a width of the Gaussian function, but there is no need to resolve a Gaussian function since the model is fixed.

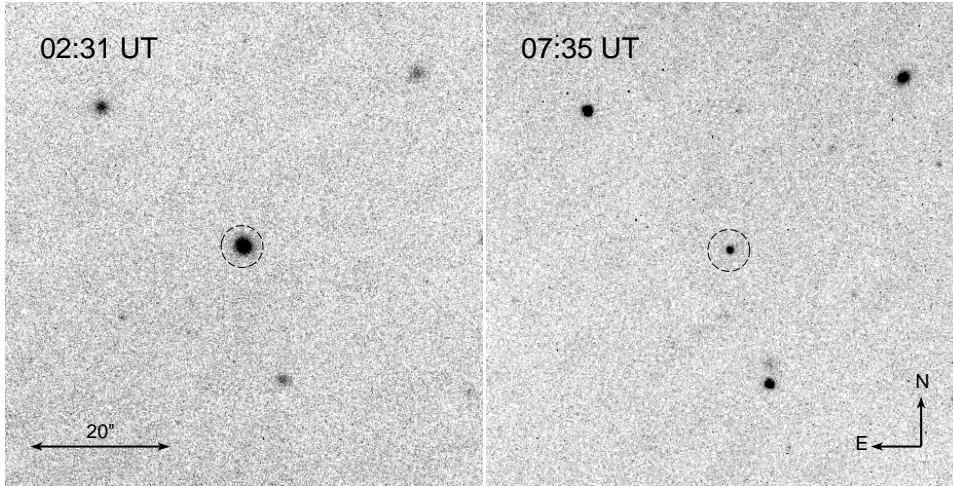
The data reduction of the whole spectrum was performed as part of a consistent and global reduction of all the X-shooter data available with our programme until 2018. A full description of the data reduction strategy is given in Selsing et al. (2019). More specifically, the RRM data were acquired and reduced in STARE mode, while the Epoch 2 observations were acquired and reduced in NOD mode (Goldoni et al. 2006; Modigliani et al. 2010). Wavelengths were corrected to the vacuum-heliocentric system.

Table 1 reports the log of the X-shooter observations, including the main observational parameters for both Epoch 1 (each set of data with a different exposure time) and Epoch 2 (each exposure had the same total exposure time of 2400 s). As shown in Table 1, the S/N of the first RRM observation of Epoch 1 is very low, so they were not included in any of the analyses reported in the following sections.

## 3. Results

Abundances of heavy elements can reveal detailed information about the metal and dust content of the ISM along the GRB sightline in the host galaxy, and also probe the close environment in which GRBs occur.

A preliminary analysis of the spectrum of GRB 160203A was included in Bolmer et al. (2019) as part of a sample study looking for molecular hydrogen in the X-shooter GRB afterglow spectra. In this work we focus on a more detailed study of the chemical abundances, metallicity of both low- and



**Fig. 2.** Acquisition images obtained in the  $r$  filter during the X-shooter observations on 3 February 2016. The left and right panels show the afterglow (circled) at the beginning of epochs 1 and 2, respectively. The fading of the GRB counterpart is apparent.

**Table 1.** Log of the X-shooter observations.

Epoch 1						
Arm	Elapsed time (s)	Exptime (s)	Airmass	Seeing	S/N	
UVB	RRM1 1109	180	1.8	0.9	4.3	
VIS	RRM1 1115	180	1.8	0.9	5.6	
NIR	RRM1 1117	180	1.8	0.9	3.7	
UVB	RRM2 1301	300	1.7	1.0	7.6	
VIS	RRM2 1385	300	1.7	1.0	8.0	
NIR	RRM2 1390	300	1.7	1.0	7.1	
UVB	RRM3 1773	600	1.6	1.1	12.7	
VIS	RRM3 1778	600	1.6	1.0	15.4	
NIR	RRM3 1782	600	1.6	1.1	11.7	
UVB	RRM4 2465	1200	1.5	1.1	17.2	
VIS	RRM4 2470	1200	1.5	1.1	19.9	
NIR	RRM4 2473	1200	1.5	1.0	14.6	
UVB	RRM5 3758	1920	1.4	0.9	20.1	
VIS	RRM5 3763	1920	1.4	0.9	22.4	
NIR	RRM5 3766	1920	1.4	1.0	11.3	
Epoch 2						
UVB	19750	2400	1.0	1.1	4.3	
VIS	19758	2400	1.0	1.0	5.8	
NIR	19761	2400	1.0	1.0	3.3	

**Notes.** Log of the X-shooter observations, including both Epoch 1 (RRM1, RRM2, RRM3, RRM4, and RRM5) and Epoch 2. The first column indicates the arm (UVB, VIS, or NIR), the next two columns are the elapsed time after the BAT trigger and the total exposure, both in seconds. The last three columns show the average airmass, seeing, and S/N per pixel ( $0.2 \text{ \AA}$  in the UVB and VIS arms,  $0.6 \text{ \AA}$  in the NIR arm).

high-ionisation absorption lines, together with the line variability of fine-structure lines.

### 3.1. Spectroscopic analysis

Figure 3 shows the X-shooter spectrum of GRB 160203A. The blue spectrum is the average of RRM3, RRM4, and RRM5

(combined to obtain the best S/N spectrum, hereafter called *Best Data*), whereas the red spectrum refers to Epoch 2 (the NIR-arm part of the spectrum has been rebinned for clarity). Identification of intervening systems were not included to avoid confusion. Some of the resonance and fine-structure lines are shown, labelled in black and red, respectively. The prominent damped Lyman- $\alpha$  (Ly- $\alpha$ ) absorption is visible in the left part of the top panel. In the top panel both the UVB and initial spectrum in the optical band are shown and in the second panel most of the high-ionisation lines in the optical band are shown. In the third panel the last part of the optical spectrum and the absorption lines in the NIR spectrum are shown, and in the bottom panel most of the absorption lines in the NIR are visible. For clarity, not all absorption line identifications are reported.

We fit the data with the Astrocook code (Cupani et al. 2020), a Python software environment to model spectral features, both in emission and absorption (with continuum and complex absorption systems).

The Ly- $\alpha$  line associated with the neutral hydrogen was located in the transition region between the UVB and VIS arms, but fortunately the HI column density was so high that both the blue and red wings of the line could be recovered. The part of the spectrum in Fig. 4 shows a strong damped Ly- $\alpha$  absorption (DLA,  $N(\text{H I}) > 2 \times 10^{20} \text{ cm}^{-2}$ ), and the red side of the Ly- $\alpha$  line constrained the best fit of the damped profile, from which we inferred a HI column density of  $\log(N(\text{H I})/\text{cm}^{-2}) = 21.75 \pm 0.10$ . We could not find any evidence for H<sub>2</sub> absorption lines.

We also identified in the spectrum several absorbing systems. We associated the highest redshift system at  $z = 3.518$  ( $z_{\text{GRB}}$ ) with the GRB 160203A host galaxy, given the presence of a damped Lyman- $\alpha$  (DLA) absorption and of fine-structure absorption lines. More specifically, the Voigt line profile computed for low-ionisation absorption lines of GRB 160203A showed at least two velocity components at  $z = 3.5176$  and  $z = 3.5189$  ( $\Delta v = 80 \text{ km s}^{-1}$ ), as shown in Fig. 5 and in Appendix A. We took the redshift of the blue component ( $z = 3.5176$ ) as that of the GRB 160203A host galaxy. High-ionisation lines like C IV and Si IV are narrower with still two components like the low-ionisation lines, but the red component is much weaker, as reported in Fig. 5.

At the GRB redshift, we detected low-ionisation absorption lines, such as S II, Si II, C II, O I, Ni II, Al II, Zn II, Cr II, Mn II, Fe II, Mg II, and Mg I. We also detected the presence of absorption features of highly ionised species, such as Al III, C IV, and

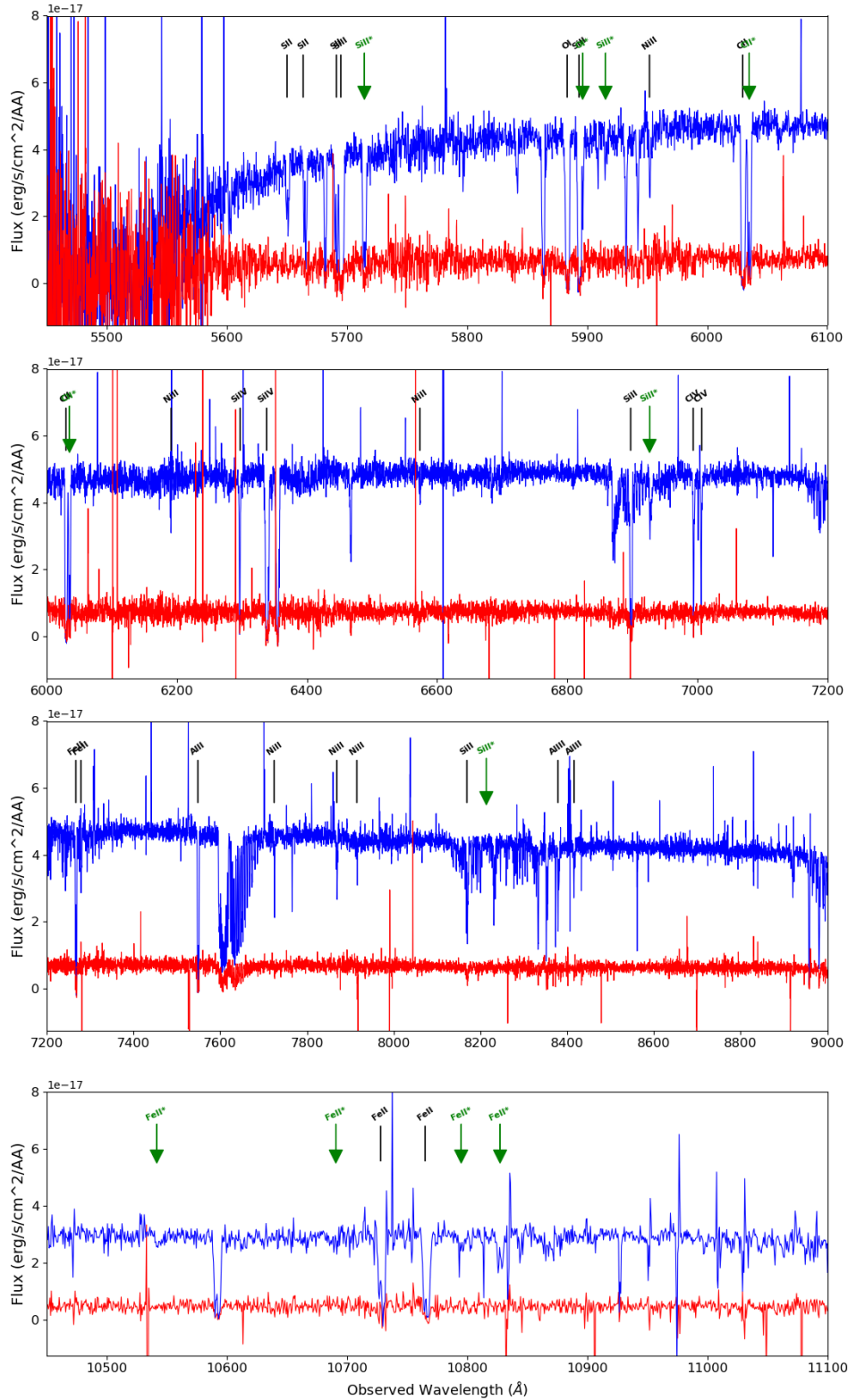


**Fig. 3.** Flux density of the UVB, VIS, and NIR X-shooter spectra for the two epochs. The average of RRM3, RRM4, and RRM5 (*Best Data*) is in blue and the Epoch 2 data is in red. Line identifications are also indicated; the fine-structure features are in green.

Si IV, and fine-structure lines, such as Si II\*, O I\*, C II\*, and Fe II\*, together with the reported resonance lines. A complete list of all the identified absorption lines and their corresponding equivalent widths (EWs) in the rest frames is reported in Table 2. The EW errors were estimated using the formula in Cayrel (1988).

In addition, we recognised six intervening systems along the GRB sightline at  $z = 1.03, 1.26, 1.98, 1.99, 2.20,$  and  $2.83$ . Due to the presence of several intervening systems, we also identified many blends with the absorption lines of the GRB host galaxy: Si II  $\lambda 1260 \text{ \AA}$  at  $z_{\text{GRB}}$  is blended with Mg II  $\lambda 2803 \text{ \AA}$  at  $z = 1.03$ ;

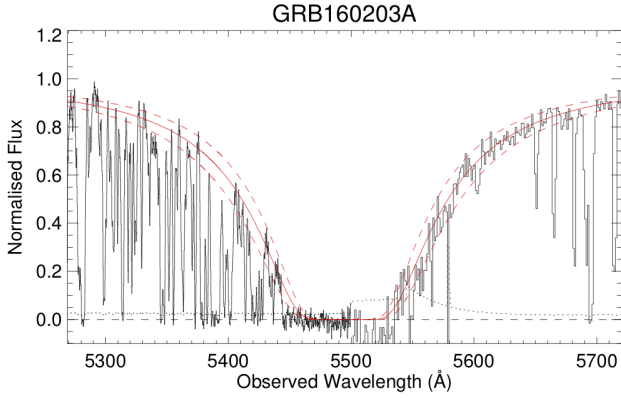


**Fig. 4.** Best fit to the damped Ly- $\alpha$  absorption line gives an H I column density of  $\log(N(\text{H I})/\text{cm}^{-2}) = 21.75 \pm 0.10$ . The noise spectrum is also shown (dotted line).

O I  $\lambda 1302 \text{ \AA}$  at  $z_{\text{GRB}}$  is blended with Mn II  $\lambda 2594 \text{ \AA}$  at  $z = 1.26$ ; Si II  $\lambda 1304 \text{ \AA}$  at  $z_{\text{GRB}}$  is blended with Fe II  $\lambda 2600 \text{ \AA}$  at  $z = 1.26$ ; Si IV  $\lambda 1402 \text{ \AA}$  at  $z_{\text{GRB}}$  is blended with Mg II  $\lambda 2796 \text{ \AA}$  at  $z = 1.26$ ; Ni II  $\lambda 1709 \text{ \AA}$  at  $z_{\text{GRB}}$  is blended with Fe II  $\lambda 2586 \text{ \AA}$  at  $z = 1.99$ ; and Zn II  $\lambda 2062 \text{ \AA}$  at  $z_{\text{GRB}}$  is blended with Cr II  $\lambda 2062 \text{ \AA}$  at  $z_{\text{GRB}}$ .

### 3.2. Column densities and metallicity

While many spectroscopic analyses of long GRBs have been performed between  $2 < z < 3$  (Krühler et al. 2015; Zafar et al. 2018; Björnsson 2019; Gatkin et al. 2019), the number of observations of long GRBs at  $z > 3.5$  is more limited. Detailed analyses of the two spectra of GRB 160203A, separated by a few hours were used not only to investigate the chemical state of the interstellar medium of the host, but also to look for fine-structure lines at high redshift and their possible temporal variability.

To compute the column densities and metallicity associated with the observed absorption lines in GRB 160203A, we used the same code, *Astrocook*, introduced in Sect. 3.1. The total column densities of low- and high-ionisation features, obtained from the line fitting are reported in Table 3 for the RRM2, RRM3, RRM4, and RRM5 data and for Epoch 2. In Appendix B we report the separated Tables (B.1–B.4) for each RRM observation, and in Table B.5 that for Epoch 2. More specifically, there are column densities for each component (together with the total) of the low-ionisation absorption lines in the top panel and the high-ionisation absorption lines in the bottom panel for RRM2, RRM3, RRM4, and RRM5, and the Epoch 2 observations, respectively. In all tables, the Doppler parameter  $b$  is provided for each component, different for the low- and high-ionisation lines.

We combined RRM3, RRM4, and RRM5 to obtain the best S/N spectrum (*Best Data*; see Section 3.1), as shown in Fig. 5, and a full illustration of all lines in Fig. A.1. We measured the column densities in order to calculate the relative abundances and the metallicities of the host galaxy. In Table 4 the three columns, after the ion identification, indicate the column densities for the two strongest absorption components at velocities  $v = 0 \text{ km s}^{-1}$  and  $v = 80 \text{ km s}^{-1}$ , and the total column densities.

The Doppler parameter for low-ionisation lines was derived from unsaturated transitions in the spectrum (e.g. Zn II  $\lambda 2026 \text{ \AA}$ ) and fixed for all other ions. Furthermore, by simultaneously fitting all the low-ionisation absorption lines leaving the value of  $b$  as a free parameter, we obtained, within the errors, the same value found from the unsaturated lines. Considering the

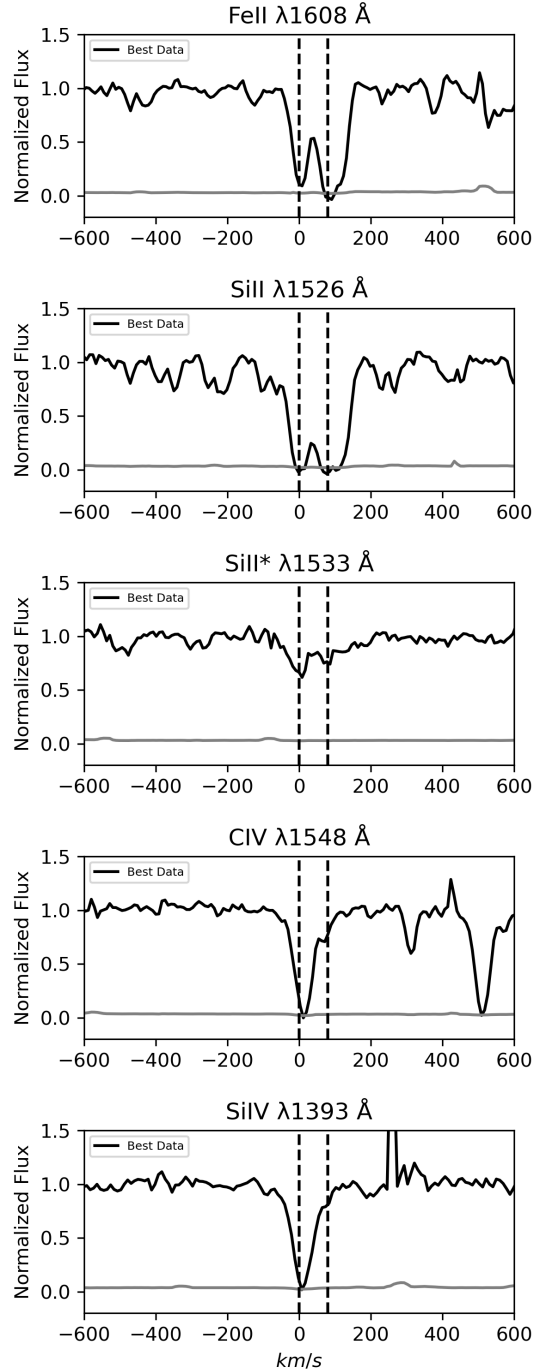


**Fig. 5.** Selection of some low-ionisation, high-ionisation, and fine-structure lines of Fe II, Si II, Si II\*, C IV, and Si IV. The two vertical lines represent the redshift of the two components inferred by low-ionisation lines (see Sect. 3.1). The data are in black and the error spectrum is in grey. The *Best Data* represents the average of RRM3, RRM4, and RRM5 spectra as described in Section 3.1 (see Fig. A.1 for all the absorption line transitions).

X-shooter resolution, hidden saturation cannot be excluded; on the other hand, considering the flux residuals and the Doppler parameter expected for warm gas ( $b \sim 10 \text{ km s}^{-1}$ , as also usually found in GRB-DLAs observed at higher resolution; Fox et al. 2008), we estimate that hidden saturation should be marginal for some of the absorption lines detected in the spectrum. In those cases, we report the respective element column densities

**Table 2.** List of identified absorption lines and rest-frame equivalent widths.

Absorption line (wavelength in Å)	EW <sub>r</sub> (Å) <i>Best Data</i>	EW <sub>r</sub> (Å) Epoch 2
S II $\lambda$ 1250.58	0.24 ± 0.03	0.13 ± 0.08
S II $\lambda$ 1253.52	0.37 ± 0.03	0.26 ± 0.08
S II $\lambda$ 1259.52	0.40 ± 0.03	0.29 ± 0.10
Si II <sup>a</sup> $\lambda$ 1260.42	<0.99	<0.80
O I <sup>a</sup> $\lambda$ 1302.17	<0.83	<0.74
Si II <sup>a</sup> $\lambda$ 1304.37	<0.89	<0.78
Ni II $\lambda$ 1317.22	0.09 ± 0.03	0.05 ± 0.08
C II $\lambda$ 1334.53	1.38 ± 0.04	1.05 ± 0.10
Ni II $\lambda$ 1370.13	0.36 ± 0.04	0.23 ± 0.10
Si IV $\lambda$ 1393.76	0.31 ± 0.04	0.21 ± 0.10
Si IV <sup>a</sup> $\lambda$ 1402.77	<1.26	<1.18
Ni II $\lambda$ 1454.84	0.08 ± 0.04	0.06 ± 0.10
Si II $\lambda$ 1526.71	0.89 ± 0.04	1.06 ± 0.15
C IV $\lambda$ 1548.20	0.34 ± 0.03	0.21 ± 0.10
C IV $\lambda$ 1550.77	0.29 ± 0.03	0.22 ± 0.10
Fe II $\lambda$ 1608.45	0.71 ± 0.03	0.50 ± 0.10
Fe II $\lambda$ 1611.20	0.13 ± 0.04	0.07 ± 0.10
Al II $\lambda$ 1670.79	0.95 ± 0.03	0.87 ± 0.10
Ni II $\lambda$ 1709.60	0.12 ± 0.04	0.08 ± 0.10
Ni II $\lambda$ 1741.55	0.16 ± 0.03	0.17 ± 0.10
Ni II $\lambda$ 1751.92	0.11 ± 0.03	0.08 ± 0.10
Si II $\lambda$ 1808.01	0.55 ± 0.05	0.42 ± 0.10
Al III $\lambda$ 1854.72	0.26 ± 0.03	0.11 ± 0.10
Al III $\lambda$ 1862.79	0.17 ± 0.03	0.12 ± 0.10
Zn II $\lambda$ 2026.14	0.37 ± 0.04	0.28 ± 0.10
Cr II $\lambda$ 2056.25	0.10 ± 0.04	0.12 ± 0.10
Zn II <sup>a</sup> $\lambda$ 2062.67	<0.46	<0.35
Fe II $\lambda$ 2344.21	1.18 ± 0.03	1.02 ± 0.15
Fe II $\lambda$ 2374.46	0.85 ± 0.03	0.68 ± 0.15
Fe II $\lambda$ 2382.77	1.29 ± 0.04	0.93 ± 0.15
Mn II $\lambda$ 2576.88	0.16 ± 0.05	0.05 ± 0.15
Fe II $\lambda$ 2586.65	1.21 ± 0.06	1.08 ± 0.15
Fe II $\lambda$ 2600.46	1.34 ± 0.05	1.26 ± 0.15
Mn II $\lambda$ 2606.46	0.08 ± 0.06	0.05 ± 0.15
Mg II $\lambda$ 2796.35	1.46 ± 0.06	1.04 ± 0.15
Mg II $\lambda$ 2803.00	1.45 ± 0.06	1.03 ± 0.15
Mg I $\lambda$ 2852.96	0.38 ± 0.05	0.30 ± 0.15

**Notes.** Identified absorption lines and rest-frame equivalent widths (EW<sub>r</sub>, in Å) measured using the IRAF package for *Best Data* (average of RRM3, RRM4, and RRM5 observations) and Epoch 2. The equivalent width errors were also computed in IRAF. Lines flagged with <sup>a</sup> are blends with intervening absorption lines, as specified in the main text.

as measurements in Tables 3 and 4, otherwise we only report the lower limits.

The heavy-element abundances that we determined for the *Best Data* are reported in Table 5. We derived zinc and sulphur abundances relative to hydrogen of  $[Zn/H] = -0.96 \pm 0.11$  and  $[S/H] = -1.21 \pm 0.10$ , respectively. We also derived the zinc abundance relative to iron of  $[Zn/Fe] < 1.15$ . Based on the absorption line from Ni II  $\lambda$ 1741 Å, we computed  $\Delta V_{90} = 198 \text{ km s}^{-1}$ , which is a measure of the width of the line that contains 90% of the optical depth (Ledoux et al. 2006). Analyses of GRB absorption lines have demonstrated that  $\Delta V_{90}$  correlates with the metallicity of the host galaxy (Arabsalmani et al. 2015).

The  $[Zn/H]$  and  $[S/H]$  values are consistent with the metallicity versus the  $\Delta V_{90}$  relation derived by Arabsalmani et al. (2015).

In general, the presence of dust may dramatically affect the observed abundances because of dust depletion (e.g. De Cia et al. 2016), so it is important to study the abundance pattern to be able to determine the total (gas+dust) metallicity, also in the neutral ISM surrounding the GRB explosion (e.g. Hartoog et al. 2015).

The abundance pattern of GRB 160203A is shown in Fig. 6. The  $x$ -axis shows the refractory index  $B2_X$  from De Cia et al. (2021), which indicates the tendency of metals to be incorporated into dust grains: on the left are refractory metals; on the right are the volatile metals, closer to the true metallicity. The  $y$ -axis is closely related to the abundances of different metals, as defined and tabulated in De Cia et al. (2021), except for carbon and aluminium, which are measured in Konstantopoulou et al. (2022). The solid line marks the linear fit of the relation  $y = [Zn/Fe]_{FIT} \times x + [M/H]_{TOT}$  to the observed abundances, as defined by De Cia et al. (2021); its normalisation determines the dust-corrected total metallicity,  $[M/H]_{TOT} = -0.78 \pm 0.13$ ; and its slope determines the overall amount of dust depletion,  $[Zn/Fe]_{FIT} = 0.69 \pm 0.15$ . We fit a linear relation to the observed abundances, considering errors along both axes and not including constraints from the limits.

#### 4. Fine-structure line variability

The GRB afterglow deposits a huge amount of UV radiation in the interstellar medium. This obviously impacts the physical condition of the gas along the GRB sightline up to a certain distance, as shown by the detection of fine-structure lines in the GRB afterglow and their time variability (Prochaska et al. 2006; Vreeswijk et al. 2007; D’Elia et al. 2009). The mechanism is known as indirect UV pumping, and consists in UV photons exciting the gas to higher energy states. The lifetime of these states is short, and therefore the atoms quickly decay to lower energy levels. The longer-lived states are either excited levels with principal quantum number  $n > 1$ , or  $n = 1$  states with higher values of spin-orbit coupling (the so-called fine-structure levels), or a combination of the two. Under particular conditions, the same mechanism could also be responsible not only for excitation, but even ionisation (Vreeswijk et al. 2013).

The comparison of observations with predictions from time-dependent photo-excitation codes has been applied to the spectrum of several GRBs (Dessauges-Zavadsky et al. 2006; D’Elia et al. 2009; Ledoux et al. 2009; De Cia et al. 2012; Hartoog et al. 2013; D’Elia et al. 2014). Estimated distances are between a few tens of parsec up to the kiloparsec scale, showing that the influence of the GRB reaches remarkable distances.

In our analysis of GRB 160203A, we noted that all the ground levels of the species commonly exhibiting fine-structure lines in GRBs (C II, O I, and Fe II) are saturated, apart from the Si II line (see Tables 3 and 4). For Si II we have reliable estimates of column density for both the ground-state and the fine-structure features, at both epochs and for both components (see Appendices). Since the fine-structure levels of Si II and Fe II are compatible with being constant, as reported in Tables 3, 4, Fig. 7, and in the Appendices, the photo-excitation code can only provide an upper limit to the source distance (see the next paragraph for a more detailed explanation). However, since the excited levels of Si II tend to remain populated even with a low flux level (see e.g. Saccardi et al. 2023), it is clear that, in this case, a distance upper limit is less constraining than that



**Table 3.** Column densities of low and high ionization absorption lines.

Absorption lines	$\log(N_{\text{RRM2}}/\text{cm}^{-2})$	$\log(N_{\text{RRM3}}/\text{cm}^{-2})$	$\log(N_{\text{RRM4}}/\text{cm}^{-2})$	$\log(N_{\text{RRM5}}/\text{cm}^{-2})$	$\log(N_{\text{Epoch 2}}/\text{cm}^{-2})$
Al II $\lambda 1670$	>14.0	>14.0	>14.0	>14.0	>13.9
C II $\lambda 1334$	>15.8	>15.9	>16.2	>16.1	>15.9
C II* $\lambda 1335$	>15.0	>15.0	>15.0	>15.1	>15.0
Fe II $\lambda 1608, \lambda 1611, \lambda 2344, \lambda 2374, \lambda 2382, \lambda 2586, \lambda 2600$	>14.9	>15.1	>15.1	>15.1	>15.2
Fe II* $\lambda 2333, \lambda 2365, \lambda 2389, \lambda 2396$	$13.68 \pm 0.15$	$13.64 \pm 0.08$	$13.56 \pm 0.07$	$13.49 \pm 0.11$	$13.5 \pm 0.3$
Mg I $\lambda 2852$		$12.60 \pm 0.09$	$12.59 \pm 0.08$	$12.46 \pm 0.13$	
Mg II $\lambda 2796, \lambda 2803$	>16.0	>15.8	>15.9	>16.0	>16.0
Ni II $\lambda 1317, \lambda 1370, \lambda 1454, \lambda 1709, \lambda 1741$		$14.06 \pm 0.06$	$14.12 \pm 0.05$	$14.06 \pm 0.05$	
O I $\lambda 1302$	>16.0	>16.0	>16.2	>16.2	>16.1
O I* $\lambda 1304$		$13.60 \pm 0.15$	$13.44 \pm 0.15$	$13.97 \pm 0.19$	
S II $\lambda 1250, \lambda 1253, \lambda 1259$	$15.61 \pm 0.14$	$15.63 \pm 0.10$	$15.63 \pm 0.10$	$15.68 \pm 0.10$	$15.8 \pm 0.2$
Si II $\lambda 1260, \lambda 1304, \lambda 1527, \lambda 1808$	$15.97 \pm 0.07$	$16.02 \pm 0.01$	$16.08 \pm 0.01$	$16.06 \pm 0.01$	$16.05 \pm 0.11$
Si II* $\lambda 1264, \lambda 1265, \lambda 1309, \lambda 1533, \lambda 1817, \lambda 1818$	$13.83 \pm 0.08$	$14.06 \pm 0.06$	$14.16 \pm 0.07$	$14.15 \pm 0.05$	$13.87 \pm 0.12$
Zn II $\lambda 2026$	$13.35 \pm 0.08$	$13.34 \pm 0.06$	$13.35 \pm 0.02$	$13.36 \pm 0.02$	$13.17 \pm 0.10$
Al III $\lambda 1854, \lambda 1862$	$13.29 \pm 0.07$	$13.32 \pm 0.04$	$13.28 \pm 0.02$	$13.22 \pm 0.02$	$13.2 \pm 0.2$
C IV $\lambda 1548, \lambda 1550$	>14.4	>14.8	>14.6	>14.6	>14.5
Si IV $\lambda 1393, \lambda 1402$	>14.1	>14.1	>14.4	>14.4	>14.4

**Notes.** Column densities of low- and high-ionisation absorption lines for the RRM2, RRM3, RRM4, and RRM5 data set (Cols. 2, 3, 4, and 5, respectively), and for the observation taken in Epoch 2 (last column).

**Table 4.** Absorption lines and column densities.

Absorption lines	$\log(N_I/\text{cm}^{-2})$	$\log(N_{II}/\text{cm}^{-2})$	$\log(N_{TOT}/\text{cm}^{-2})$
Al II $\lambda 1670$	>13.6	>13.8	>14.0
C II $\lambda 1334$	>16.0	>15.6	>16.2
C II* $\lambda 1335$	>14.8	>14.8	>15.1
Cr II $\lambda 2017, \lambda 2056$	$13.55 \pm 0.07$	$13.72 \pm 0.05$	$13.94 \pm 0.04$
Fe II $\lambda 1608, \lambda 1611, \lambda 2344, \lambda 2374, \lambda 2382, \lambda 2586, \lambda 2600$	>14.61	$15.01 \pm 0.03$	>15.14
Fe II* $\lambda 2333, \lambda 2365, \lambda 2389, \lambda 2396$	$13.23 \pm 0.11$	$13.29 \pm 0.09$	$13.56 \pm 0.07$
Mg I $\lambda 2852$	$12.25 \pm 0.13$	$12.25 \pm 0.09$	$12.55 \pm 0.08$
Mg II $\lambda 2796, \lambda 2803$	>16.1	>15.0	>16.1
Mn II $\lambda 2576, \lambda 2594, \lambda 2606$	>12.8	>13.3	>13.4
Ni II $\lambda 1317, \lambda 1370, \lambda 1454, \lambda 1709, \lambda 1741$	$13.57 \pm 0.05$	$14.12 \pm 0.05$	$14.22 \pm 0.02$
O I $\lambda 1302$	>15.8	>15.9	>16.2
O I* $\lambda 1304$		$13.77 \pm 0.19$	$13.77 \pm 0.19$
S II $\lambda 1250, \lambda 1253, \lambda 1259$	$15.25 \pm 0.04$	$15.44 \pm 0.04$	$15.66 \pm 0.03$
Si II $\lambda 1260, \lambda 1304, \lambda 1527, \lambda 1808$	$15.65 \pm 0.02$	$15.78 \pm 0.02$	$16.02 \pm 0.02$
Si II* $\lambda 1264, \lambda 1265, \lambda 1309, \lambda 1533, \lambda 1817, \lambda 1818$	$13.96 \pm 0.04$	$13.71 \pm 0.04$	$14.15 \pm 0.03$
Zn II $\lambda 2026$	$12.74 \pm 0.03$	$13.22 \pm 0.02$	$13.35 \pm 0.02$
$b$ (km s <sup>-1</sup> )	$20 \pm 2$	$33 \pm 2$	
Al III $\lambda 1854, \lambda 1862$	$13.10 \pm 0.02$	$12.80 \pm 0.04$	$13.28 \pm 0.02$
C IV $\lambda 1548, \lambda 1550$	>14.7	>13.3	>14.8
Si IV $\lambda 1393, \lambda 1402$	>14.5	>12.7	>14.5
$b$ (km s <sup>-1</sup> )	$17 \pm 2$	$26 \pm 2$	

**Notes.** Low- and high-ionisation absorption lines (first column), column densities of the two strongest components (second and third columns), and the corresponding total column densities of *Best Data*, obtained by combining the single exposure with the best S/N, i.e. RRM3, RRM4, and RRM5 observations.

obtained with Fe II. This is why in the following we focus on Fe II.

Even if Fe II ground-state features are saturated, one can nevertheless attempt to fit the fine-structure column densities of the different observations, leaving the initial column density of the system as a free parameter. The results (Table 3) indicate that these columns are compatible with being constant in the time interval between 18 minutes and 5.7 hours after the burst alert,

although Epoch 2 is affected by a large uncertainty (see also Table 6, in which fine-structure line EWs in the two epochs do not show strong variations). In order to obtain a nearly constant fine-structure line column density in the UV pumping scenario, the absorber must be close enough to the GRB to keep the flux level sufficiently high for a long time.

This occurs because the maximum value achievable by the ratio of the Fe II fine structure to ground level is 8/10. This is

**Table 5.** Heavy element abundances.

Element	[X/H]
Al	$> -2.17$
C	$> -1.98$
Cr	$-1.45 \pm 0.12$
Fe	$> -2.09$
Mg	$> -1.25$
Mn	$> -1.80$
Ni	$-1.75 \pm 0.11$
O	$> -2.27$
S <sup>(†)</sup>	$-1.21 \pm 0.10$
Si <sup>(†)</sup>	$-1.24 \pm 0.10$
Zn <sup>(†)</sup>	$-0.96 \pm 0.11$

**Notes.** Heavy element abundances relative to hydrogen [X/H] in the ISM measured from the GRB 160203A afterglow spectrum *Best Data*.  
<sup>(†)</sup> Hidden saturation cannot be excluded, but it is unlikely; see Sect. 3.2.

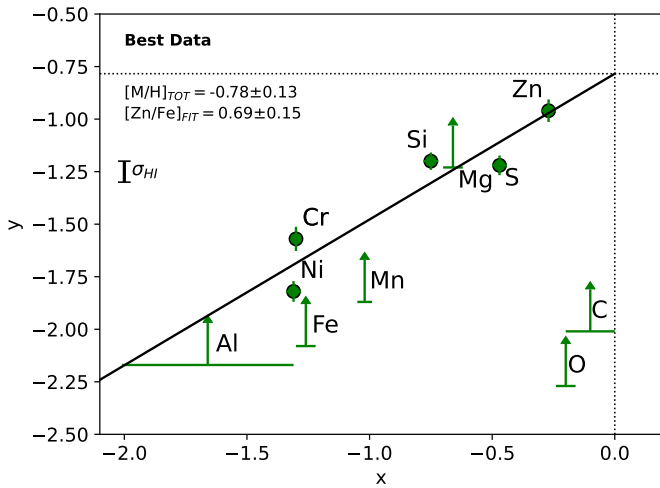


**Fig. 6.** *Best data* observed abundance pattern. The  $x$ -axis shows the refractory index  $B2_x$  from De Cia et al. (2021), while the  $y$ -axis is closely related to the observed abundances. The solid line shows the linear fit of the relation  $y = [\text{Zn}/\text{Fe}]_{\text{FIT}} \times x + [\text{M}/\text{H}]_{\text{TOT}}$  to the observed abundances, not including the constraints from the limits.

the ratio between the  $2J + 1$  quantum values of the  $J = 7/2$  fine-structure level and  $J = 9/2$  for the ground-state level. Once this maximum is reached, no matter if the flux experienced by the absorbing gas increases, this ratio would stay the same. Thus, we check if the absorber could lie at a distance from the GRB at which the experienced flux was able to keep this ratio value at its maximum, up to the second X-shooter observation. In this way we can explain the non-variability of the fine-structure line, and eventually obtain upper limits to the GRB-absorber distance. At larger distances, the fine-structure to ground-state ratio would decrease during the two observations.

This statement can be quantified with the above-mentioned photo-excitation code. We adopt the Fe II\* column densities in Table B.1, B.2, B.3, B.4, and B.5, with a range of Doppler parameters determined from absorption-line best fits, and let the Fe II ground state free to vary. Physically, the latter assumption means we are assuming that the iron contributing to the absorption is split in two regions, blended in our spectra. One of these is far from the GRB and is completely in the ground state. It contains most of the iron. The other is the target of the photo-excitation

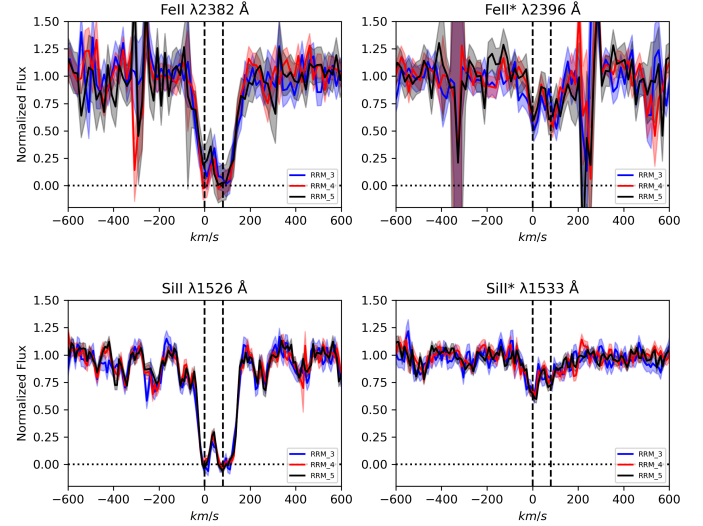


**Fig. 7.** Resonance and fine-structure lines of Fe II (top) and Si II (bottom). The blue spectrum refers to RRM3, the red spectrum refers to RRM4, and the black line refers to RRM5. The shaded area around the solid lines represents the error spectra for each RRM.

**Table 6.** Fine structure EW.

Line	$\text{EW}_r$ (Å) <i>Best Data</i>	$\text{EW}_r$ (Å) Epoch 2
Si II* $\lambda 1264.74$ Å	$0.65 \pm 0.03$	$0.57 \pm 0.10$
Si II* $\lambda 1309.28$ Å	$0.12 \pm 0.04$	$0.08 \pm 0.11$
C II* $\lambda 1335.71$ Å	$0.63 \pm 0.03$	$0.54 \pm 0.12$
Si II* $\lambda 1533.43$ Å	$0.22 \pm 0.03$	$0.20 \pm 0.12$
Si II* $\lambda 1817.45$ Å	$0.11 \pm 0.03$	$0.09 \pm 0.10$
Fe II* $\lambda 2332.02$ Å	$0.31 \pm 0.06$	$0.18 \pm 0.12$
Fe II* $\lambda 2365.55$ Å	$0.10 \pm 0.07$	$0.08 \pm 0.15$
Fe II* $\lambda 2389.36$ Å	$0.17 \pm 0.06$	$0.18 \pm 0.13$
Fe II* $\lambda 2396.35$ Å	$0.46 \pm 0.05$	$0.28 \pm 0.15$
Fe II* $\lambda 2399.98$ Å	$0.19 \pm 0.05$	$0.18 \pm 0.15$
Fe II* $\lambda 2407.39$ Å	$0.21 \pm 0.06$	$0.15 \pm 0.15$

**Notes.** Rest-frame equivalent width ( $\text{EW}_r$ ) of fine-structure lines for *Best Data* (average of RRM3, RRM4, and RRM5 observations) and Epoch 2. The errors were computed via the formula in Cayrel (1988).

code. It shows the Fe II\* absorption and is closer, allowing the indirect UV pumping to be at work. This region is exposed to a strong flux, allows a Fe II\*/Fe II ratio close to 0.8, and consequently a (nearly) constant Fe II\* column density throughout the X-shooter observations. Leaving the Fe II ground-state column free to vary allows the model to obtain the correct normalisation to fit the data. This results in a distance upper limit since every other fit with a lower distance is “flatter” and is equally good. The above assumption was made for both components I and II of GRB 160203A. We determined upper limits to the distance between the GRB and the absorber  $d < 200$  pc and  $d < 300$  pc for component I and II, respectively (see Fig. 8). These upper limits are at the  $1\sigma$  level, and correspond to the allowed  $1\sigma$  uncertainties of the measured column densities. These distances are consistent with the values found in other GRBs (see e.g. Hartoog et al. 2013), making the UV pumping a viable explanation for the presence of fine-structure lines. Photoionisation

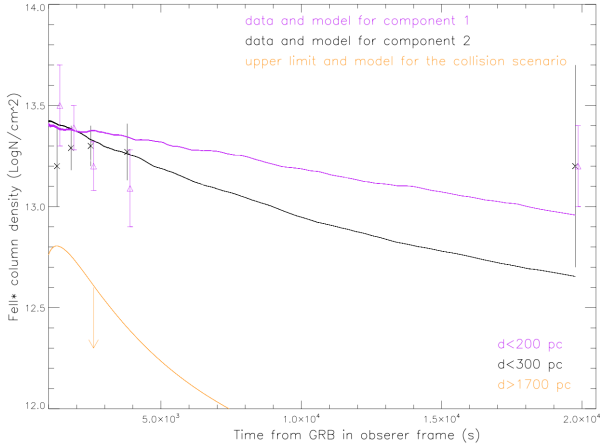


**Fig. 8.** Comparison between the photo-excitation code and data for the Fe II\* column densities reported in Tables B.1, B.2, B.3, B.4, and B.5. We derive a GRB–absorber distance upper limit of 200 pc and 300 pc for Component I (purple) and II (black), respectively. For clarity reasons, the purple points have been slightly shifted to the right. Assuming that fine structures are produced by collisions instead of UV pumping, we derived a lower limit to the distance of  $d > 1700$  pc for both components (model and column upper limit are in yellow).

should not be an issue here, despite the distances involved. Indeed, GRB 080310 is the only burst for which photoionisation of Fe II into Fe III has been detected (De Cia et al. 2012; Vreeswijk et al. 2013). The peculiarity of this GRB is due to its low HI column density, with  $\log(N(\text{HI})/\text{cm}^{-2}) = 18.75$ . Values two orders of magnitude larger would have been high enough to allow HI to efficiently shield the iron and prevent photoionisation (De Cia et al. 2012; Vreeswijk et al. 2013). We note that GRB 160203A has a HI column density that is  $10^3$  times that of GRB 080310.

We also explore the scenario in which fine-structure lines are produced by collisions instead of UV pumping. Thus, we compute an upper limit to the UV pumping Fe II\* column density using the combined RRM3+RRM4+RRM5 spectrum, the one with the high S/N (*Best Data*). The result is  $\text{Log}(N \text{ Fe II}^*/\text{cm}^2) = 12.6$ . This value, together with the ground-state column density of the Fe II reported in Table 4 for component II, was used for comparison with the photo-excitation code and to obtain a lower limit to the GRB–absorber distance in the case of collisions. We obtained  $d > 1700$  pc for both components (see again Fig. 8).

If collisions dominate over photo excitation, one can use the numerical solution provided by Prochaska et al. (2006) for the dependency of  $n_e$  on the Fe II\*/Fe II ratio (together with that for the Si II\*/Si II ratio; see their Fig. 9). We obtain  $n_e \sim 5 \text{ cm}^{-3}$  for Si II and  $n_e \sim 200 \text{ cm}^{-3}$  for Fe II. This discrepancy (which would hold even using a temperature different from 2600 K, adopted by Prochaska et al. 2006 in their Fig. 9) would be even larger for a higher Fe II\*/Fe II ratio, which is probably underestimated (see Tables 7–10). In conclusion, the collision scenario needs more assumptions to work, just as for the photo-excitation mechanism.

Considering that no conclusive detection of gas excited by collisions in GRBs has been reported yet, while photo-excitation has been proved to be a valid mechanism to explain the fine-structure lines detected in the studies of other GRBs (Prochaska et al. 2006; Dessauges-Zavadsky et al. 2006; Vreeswijk et al. 2007; D’Elia et al. 2009; Ledoux et al. 2009; De Cia et al. 2012; Hartoog et al. 2013; D’Elia et al. 2014), we prefer photo-excitation as the viable mechanism to produce the fine-structure lines in GRB 160203A. Even though we need to fine-tune the

Fe II ground-state column density, the computed distances are compatible with those reported for other bursts, and the HI column density is high enough to shield the Fe II and prevent photo-ionisation into Fe III. Nevertheless, the data quality is not high enough to rule out other explanations. The collisional excitation is still possible, despite the need for further assumptions (as in the photo-excitation scenario), to explain the observations.

## 5. Discussion

Velocity components and measurements of line EWs can provide strong indications of the structure of the gas of the host galaxy along the line of sight to the GRB (Küpcü Yoldaş et al. 2007; Margutti et al. 2007; Thöne et al. 2008; Arabsalmani et al. 2015; Friis et al. 2015). The line profile computed for the ionisation lines of GRB 160203A, even if saturated, shows at least two velocity components, indicating the presence of no fewer than two gas clouds along the line of sight of the afterglow. This is clearly visible in the Voigt profiles shown in Appendix A and also in Fig. 7, where the low-ionisation lines (e.g. Si II and Fe II) show two distinct velocity components. The blue and the red components have a relative velocity equal to  $0 \text{ km s}^{-1}$  and  $80 \text{ km s}^{-1}$  from the  $z = 3.5176$  position of the blue component, respectively.

High-ionisation lines (e.g. C IV and Si IV) still show two components, as do the low-ionisation lines, with the red component much weaker, as presented in Fig. 5 and in the plots in Appendix A. Overall, the two components of the high-ionisation transitions have velocities coincident with those of the low-ionisation lines, and as reported in Fig. A.1 the stronger component of the high-ionisation lines also coincides with the stronger component of the fine-structure lines, but not that of the ground-state of the low-ionisation lines.

Taking into consideration that both the low- and high-ionisation lines have consistent velocities, this could suggest that the cold and hot gas detected along the line of sight of GRB 160203A are in a similar region of its host galaxy. Typically, when the high-ionisation lines have a different profile than the low-ionisation species, one could infer that they are associated with the circumgalactic medium (CGM), and related with turbulent motion or the coupling between gas and dust (Prochaska et al. 2009; Juvella & Ysard 2011). In the case of GRB 160203A, we reported high-ionisation lines with a weaker component at  $80 \text{ km s}^{-1}$ , and this could indicate that these species are associated with a cooler ionised gas.

From the analysis of the column densities of the fine-structure lines in Epoch 1 and in Epoch 2, we could not detect significant variability, indicating that, in the UV pumping scenario, the absorber should be close enough to GRB 160203A to allow the GRB flux being rather constant between the first and the second epoch of our observations. In detail, we computed an upper limit of 200 pc and 300 pc for component I and II, respectively. Such values are well within the range of what is found in the literature for similar studies. The data cannot conclusively rule out that fine-structure lines are produced by collisions instead of UV pumping. In this scenario, we determined a lower limit of the GRB–absorber distance of  $d > 1700$  pc for both components and an electron density in the range  $1\text{--}200/\text{cm}^3$ . This wide range of  $n_e$  reflects a discrepancy that arises when one uses the Fe II\*/Fe II or the Si II\*/Si II ratio. Further assumptions are needed to mitigate this discrepancy.

GRB 160203A is not the only event for which our collaboration had the opportunity to look for fine-structure line variability between two following observations. GRB 100901A (Hartoog et al. 2013) and GRB 120327A (D’Elia et al. 2014) are successful examples for which we could derive the distance of the absorbers from the GRB using the UV pumping mechanism, measuring a variability within time internals of 1–168 hours and 25.62 hours, respectively. Both these GRBs were at a lower redshift, GRB 100901A at  $z = 1.41$  and GRB 120327A at  $z = 2.81$ , and for this reason they were also detected by the Ultraviolet and the Optical Telescope (UVOT) instrument on *Swift* ( $U = 17.52$  and  $U = 18.02$ , respectively).

Given the higher redshift, the BAT instrument on *Swift* reported a lower fluence for GRB 160203A, compared to the other two events, and the *Swift*/UVOT could not detect it ( $U > 19.5$ ). An interesting difference in these events is that both GRB 100901A and 120327A show a variability of the fine-structure features, while they are constant within the errors in GRB 160203A. This result is still consistent with an indirect UV pumping scenario, provided that the flux experienced by the intervening gas is high enough to keep these lines near to their maximum allowed value during the whole spectroscopic campaign. This requirement can be met if the intrinsic GRB luminosity is high enough and/or the absorber is sufficiently close to the GRB.

Another goal of the spectral analysis of long GRBs was to increase the population of host galaxies at high redshift for which we were able to determine a metallicity and use this information to study the properties of the interstellar medium of late-galaxies (Schady 2017). The GRB metallicities and their evolution in time are overall consistent with Quasars-DLAs (Rafelski et al. 2012; De Cia 2018), where the decrease in metal abundance with increasing  $z$  is clearer because of the larger number of systems. The metallicity of GRB 160203A is consistent with the general indication that GRB host galaxies have lower metal abundances at higher redshift (Fynbo et al. 2008; Levesque et al. 2010; Savaglio 2012; Krühler et al. 2015).

## 6. Conclusion

As part of the VLT/X-shooter/Stargate programme, we observed several GRBs at a redshift similar to that of GRB 160203A. During the X-shooter science verification, GRB 090313 was detected at  $z = 3.373$  (de Ugarte Postigo et al. 2010; D’Elia et al. 2010), showing absorption features, S II, Si II, O I, Si IV, C IV, Fe II, just like those of GRB 130408A at  $z = 3.758$  (Hjorth et al. 2013) and GRB 170202A at  $z = 3.645$  (Palmerio et al. 2017). Moreover, we also observed a few GRBs for which we detected emission lines from the [O III] doublet, such as GRB 110818A at  $z = 3.36$  (D’Avanzo et al. 2011), GRB 111123A at  $z = 3.151$  (Xu et al. 2013), and GRB 121201A at  $z = 3.385$ , that showed Ly- $\alpha$  emissions (Sanchez-Ramirez et al. 2012). Unfortunately, we had no opportunity to perform a second set of observations within a few hours for any of these GRBs at a similar redshift, which would have allowed us to study the evolution of the detected features. GRB 160203A provided this opportunity, and made it possible to check for fine-structure line variability during two close observing epochs (Dessauges-Zavadsky et al. 2006; Hartoog et al. 2013).

From the study presented here we emphasise the following points:

- The optical and near-infrared spectra with VLT/X-shooter were obtained in RRM (five observations, reported as

Epoch 1) just 18 minutes after the  $\gamma$ -ray alert, together with a second set of observations (Epoch 2) about 5.7 hours after the alert. We investigated the properties of the gas along the line of sight of GRB 160203A and we detected neutral hydrogen, low-ionisation, high-ionisation, and fine-structure metal lines, from the GRB host galaxy at redshift  $z = 3.518$ . We also detected absorption lines from six intervening systems along the GRB line of sight, at  $z = 1.03, 1.26, 1.98, 1.99, 2.20, 2.83$ .

- GRB 160203A shows a high HI column density with respect to the DLAs of other GRBs at similar redshifts,  $\log(N(\text{HI})/\text{cm}^{-2}) = 21.75 \pm 0.10$ , and a metal content normal for its redshift, indicating that the region in which the GRB occurred had a high hydrogen content. The work by Ranjan et al. (2020) showed a strong similarity between the DLAs associated with long GRBs and the population of extremely strong DLAs associated with quasars with HI column densities between  $\log N(\text{HI}/\text{cm}^{-2}) = 21.6$  and  $\log N(\text{HI}/\text{cm}^{-2}) = 22.4$ . The measured HI column density of GRB 160203A belongs to this range and gives a further indication of the similarity between the environments of the two DLA populations.
  - The data show no evidence for H<sub>2</sub> absorption lines and a lack of molecular gas (see Heintz et al. 2019 on the C I–H<sub>2</sub> connection).
  - We performed a detailed analysis of each observation to investigate the chemical properties of the ISM of the host galaxy and to look for fine-structure line variability. We found a dust-corrected metallicity of  $[M/H]_{\text{TOT}} = -0.78 \pm 0.13$ , and overall strength of the dust depletion  $[Zn/Fe]_{\text{FIT}} = 0.69 \pm 0.15$ .
  - Low-ionisation absorption lines show a width that is consistent with the GRB metallicity, while the high-ionisation lines exhibit a remarkable narrow structure compared to other GRBs previously studied, and similarly seen in the QSO-DLAs sample by Heintz et al. (2018). The line profile computed for both the low- and high-ionisation lines of GRB 160203A shows at least two components, with coincident velocities.
  - From the modelling of the fine-structure lines we tried to estimate the distance of the absorbing gas clouds. The small variation (if any) of the Fe II fine-structure line, together with the lack of a reliable value for the corresponding ground-state column density, did not allow a firm estimate of the distance at which the related absorbing gas should be located, assuming a UV pumping model. Nevertheless, an upper limit of  $d < 200$  ( $d < 300$ ) pc for component I (II) can be estimated. These values do not conflict with previous determinations of the same quantity for other GRBs (Hartoog et al. 2013), making UV pumping a viable explanation for the presence of fine-structure lines in GRB 160203A. Nevertheless, although we prefer the photo-excitation scenario, the data quality is not high enough to conclusively rule out collisions as the mechanism to produce fine-structure lines. In this case, we can determine a lower limit to the GRB–absorber distance of  $d > 1700$  pc for both components.
- Overall, the observations and corresponding spectral and photometric analysis of GRB 160203A confirmed the effectiveness of using GRBs as a tool to study the chemical composition of galaxies at high redshift and highlights the value of rapid multi-epoch follow-up of GRBs.

**Acknowledgements.** Based on observations collected at the European Organisation for Astronomical Research in the Southern Hemisphere under ESO programme 096.A-0079, PI: J.P.U.Fynbo. This work made use of data collected by the *Swift* satellite. The Cosmic Dawn Center (DAWN) is funded by the Danish National Research Foundation under grant No. 140. G.P. thanks the Swinburne University of Technology for their support as one of their seasonal teaching staff. A.S. and S.D.V. acknowledge support from CNES and DIM-ACAV+. K.E.H. acknowledges support from the Carlsberg Foundation Reintegration Fellowship Grant CF21-0103. A.D.C. acknowledges support by the Swiss National Science Foundation under grant 185692. D.A.K. acknowledges support from Spanish National Research Project RTI2018-098104-J-I00 (GRBPhot). D.B.M. is supported by the European Research Council (ERC) under the European Union's Horizon 2020 research and innovation programme (grant agreement No. 725246).

## References

- Arabsalmani, M., Møller, P., Fynbo, J. P. U., et al. 2015, *MNRAS*, **446**, 990
- Bégué, D., & Pe'er, A. 2015, *ApJ*, **802**, 134
- Björnsson, G. 2019, *ApJ*, **887**, 219
- Bolmer, J., Ledoux, C., Wiseman, P., et al. 2019, *A&A*, **623**, A43
- Breeveld, A. A., & D'Avanzo, P. 2016, *GRB Coordinates Network*, **18984**, 1
- Butler, N., Watson, A. M., Kutuyrev, A., et al. 2016, *GRB Coordinates Network*, **18989**, 1
- Campana, S., Lazzati, D., Ripamonti, E., et al. 2007, *ApJ*, **654**, L17
- Cano, Z., Izzo, L., de Ugarte Postigo, A., et al. 2017, *A&A*, **605**, A107
- Cayrel, R. 1988, *IAU Symp.*, **132**, 345
- Christensen, L., Vergani, S. D., Schulze, S., et al. 2017, *A&A*, **608**, A84
- Cucchiara, A., Levan, A. J., Fox, D. B., et al. 2011, *ApJ*, **736**, 7
- Cucchiara, A., Fumagalli, M., Rafelski, M., et al. 2015, *ApJ*, **804**, 51
- Cucchiara, A., Totani, T., & Tanvir, N. 2016, *Space Sci. Rev.*, **202**, 143
- Capani, G., D'Odorico, V., Cristiani, S., et al. 2020, *SPIE Conf. Ser.*, **11452**, 114521U
- D'Avanzo, P., Sparre, M., Watson, D., et al. 2011, *GRB Coordinates Network*, **12284**, 1
- D'Avanzo, P., Barthelmy, S. D., Burrows, D. N., et al. 2016, *GRB Coordinates Network*, **18979**, 1
- De Cia, A. 2018, *A&A*, **613**, L2
- De Cia, A., Ledoux, C., Fox, A. J., et al. 2012, *A&A*, **545**, A64
- De Cia, A., Ledoux, C., Mattsson, L., et al. 2016, *A&A*, **596**, A97
- De Cia, A., Jenkins, E. B., Fox, A. J., et al. 2021, *Nature*, **597**, 206
- D'Elia, V., Fiore, F., Perna, R., et al. 2009, *ApJ*, **694**, 332
- D'Elia, V., Fynbo, J. P. U., Covino, S., et al. 2010, *A&A*, **523**, A36
- D'Elia, V., Campana, S., Covino, S., et al. 2011, *MNRAS*, **418**, 680
- D'Elia, V., Fynbo, J. P. U., Goldoni, P., et al. 2014, *A&A*, **564**, A38
- Dessauges-Zavadsky, M., Chen, H.-W., Prochaska, J. X., Bloom, J. S., & Barth, A. J. 2006, *ApJ*, **648**, L89
- de Ugarte Postigo, A., Goldoni, P., Thöne, C. C., et al. 2010, *A&A*, **513**, A42
- de Ugarte Postigo, A., Thöne, C. C., Bolmer, J., et al. 2018, *A&A*, **620**, A119
- Elliott, J., Greiner, J., Khochfar, S., et al. 2012, *A&A*, **539**, A113
- Evans, P. A., Beardmore, A. P., Page, K. L., et al. 2009, *MNRAS*, **397**, 1177
- Fox, A. J., Ledoux, C., Vreeswijk, P. M., Smette, A., & Jaunsen, A. O. 2008, *A&A*, **491**, 189
- Friis, M., De Cia, A., Krühler, T., et al. 2015, *MNRAS*, **451**, 167
- Fynbo, J. P. U., Starling, R. L. C., Ledoux, C., et al. 2006, *A&A*, **451**, L47
- Fynbo, J. P. U., Prochaska, J. X., Sommer-Larsen, J., Dessauges-Zavadsky, M., & Møller, P. 2008, *ApJ*, **683**, 321
- Gatkin, P., Veilleux, S., & Cucchiara, A. 2019, *ApJ*, **884**, 66
- Gehrels, N., & Razzaque, S. 2013, *Front. Phys.*, **8**, 661
- Gehrels, N., Chincarini, G., Giommi, P., et al. 2004, *ApJ*, **611**, 1005
- Goldoni, P., Royer, F., François, P., et al. 2006, *SPIE Conf. Ser.*, **6269**, 80
- Greiner, J., Bornemann, W., Clemens, C., et al. 2008, *PASP*, **120**, 405
- Hartoog, O. E., Wiersema, K., Vreeswijk, P. M., et al. 2013, *MNRAS*, **430**, 2739
- Hartoog, O. E., Malesani, D., Fynbo, J. P. U., et al. 2015, *A&A*, **580**, A139
- Heintz, K. E., Watson, D., Jakobsson, P., et al. 2018, *MNRAS*, **479**, 3456
- Heintz, K. E., Ledoux, C., Fynbo, J. P. U., et al. 2019, *A&A*, **621**, A20
- Hjorth, J., Melandri, A., Malesani, D., Kruehler, T., & Xu, D. 2013, *GRB Coordinates Network*, **14365**, 1
- Juvela, M., & Ysard, N. 2011, *ApJ*, **739**, 63
- Konstantopoulou, C., De Cia, A., Krogager, J.-K., et al. 2022, *A&A*, **666**, A12
- Kruehler, T., Kann, D. A., Greiner, J., & Bolmer, J. 2016, *GRB Coordinates Network*, **18980**, 1
- Krühler, T., Ledoux, C., Fynbo, J. P. U., et al. 2013, *A&A*, **557**, A18
- Krühler, T., Malesani, D., Fynbo, J. P. U., et al. 2015, *A&A*, **581**, A125
- Küpcü Yıldız, A., Salvato, M., Greiner, J., et al. 2007, *A&A*, **463**, 893
- Ledoux, C., Petitjean, P., Fynbo, J. P. U., Møller, P., & Srianand, R. 2006, *A&A*, **457**, 71
- Ledoux, C., Vreeswijk, P. M., Smette, A., et al. 2009, *A&A*, **506**, 661
- Levan, A. J., Gompertz, B. P., Salafia, O. S., et al. 2024, *Nature*, **626**, 737
- Levesque, E. M., Soderberg, A. M., Kewley, L. J., & Berger, E. 2010, *ApJ*, **725**, 1337
- Margutti, R., Chincarini, G., Covino, S., et al. 2007, *A&A*, **474**, 815
- Modigliani, A., Goldoni, P., Royer, F., et al. 2010, *Proc. SPIE*, **7737**, 773728
- Nagamine, K., Zhang, B., & Hernquist, L. 2008, *ApJ*, **686**, L57
- Osborne, J. P., Page, K. L., D'Elia, V., et al. 2016, *GRB Coordinates Network*, **18986**
- Palmerio, J., Kruehler, T., Malesani, D., & Fynbo, J. P. U. 2017, *GRB Coordinates Network*, **20589**, 1
- Palmerio, J. T., Vergani, S. D., Salvaterra, R., et al. 2019, *A&A*, **623**, A26
- Piranomonte, S., Japelj, J., Vergani, S. D., et al. 2015, *MNRAS*, **452**, 3293
- Prochaska, J. X., Chen, H.-W., & Bloom, J. S. 2006, *ApJ*, **648**, 95
- Prochaska, J. X., Dessauges-Zavadsky, M., Ramirez-Ruiz, E., & Chen, H.-W. 2008, *ApJ*, **685**, 344
- Prochaska, J. X., Sheffer, Y., Perley, D. A., et al. 2009, *ApJ*, **691**, L27
- Pugliese, G., Covino, S., Kruehler, T., Xu, D., & Tanvir, N. R. 2016, *GRB Coordinates Network*, **18982**, 1
- Rafelski, M., Wolfe, A. M., Prochaska, J. X., Neeleman, M., & Mendez, A. J. 2012, *ApJ*, **755**, 89
- Ranjan, A., Noterdaeme, P., Krogager, J. K., et al. 2020, *A&A*, **633**, A125
- Rastinejad, J. C., Gompertz, B. P., Levan, A. J., et al. 2022, *Nature*, **612**, 223
- Saccardi, A., Vergani, S. D., De Cia, A., et al. 2023, *A&A*, **671**, A84
- Salvaterra, R., Della Valle, M., Campana, S., et al. 2009, *Nature*, **461**, 1258
- Salvaterra, R., Campana, S., Vergani, S. D., et al. 2012, *ApJ*, **749**, 68
- Sanchez-Ramirez, R., de Ugarte Postigo, A., Kruehler, T., et al. 2012, *GRB Coordinates Network*, **14035**, 1
- Savaglio, S. 2012, *Astron. Nachr.*, **333**, 480
- Savaglio, S., Fall, S. M., & Fiore, F. 2003, *ApJ*, **585**, 638
- Schady, P. 2015, *J. High Energy Astrophys.*, **7**, 56
- Schady, P. 2017, *R. Soc. Open Sci.*, **4**, 170304
- Selsing, J., Malesani, D., Goldoni, P., et al. 2019, *A&A*, **623**, A92
- Sparre, M., Hartoog, O. E., Krühler, T., et al. 2014, *ApJ*, **785**, 150
- Tanvir, N. R., Fox, D. B., Levan, A. J., et al. 2009, *Nature*, **461**, 1254
- Tanvir, N. R., Levan, A. J., Fruchter, A. S., et al. 2012, *ApJ*, **754**, 46
- Tanvir, N. R., Laskar, T., Levan, A. J., et al. 2018, *ApJ*, **865**, 107
- Tanvir, N. R., Fynbo, J. P. U., de Ugarte Postigo, A., et al. 2019, *MNRAS*, **483**, 5380
- Thöne, C. C., Wiersema, K., Ledoux, C., et al. 2008, *A&A*, **489**, 37
- Thöne, C. C., Fynbo, J. P. U., Goldoni, P., et al. 2013, *MNRAS*, **428**, 3590
- Trotter, A., Reichart, D., Haislip, J., et al. 2016, *GRB Coordinates Network*, **18987**, 1
- Vernet, J., Dekker, H., D'Odorico, S., et al. 2011, *A&A*, **536**, A105
- Vreeswijk, P. M., Ledoux, C., Smette, A., et al. 2007, *A&A*, **468**, 83
- Vreeswijk, P. M., Ledoux, C., Raassen, A. J. J., et al. 2013, *A&A*, **549**, A22
- Wiseman, P., Schady, P., Bolmer, J., et al. 2017, *A&A*, **599**, A24
- Xu, D., Malesani, D., Kruehler, T., et al. 2013, *GRB Coordinates Network*, **14273**, 1
- Zafar, T., Møller, P., Watson, D., et al. 2018, *MNRAS*, **480**, 108

**Appendix A: Voigt profiles of low- and high-ionisation, and fine-structure metal lines**

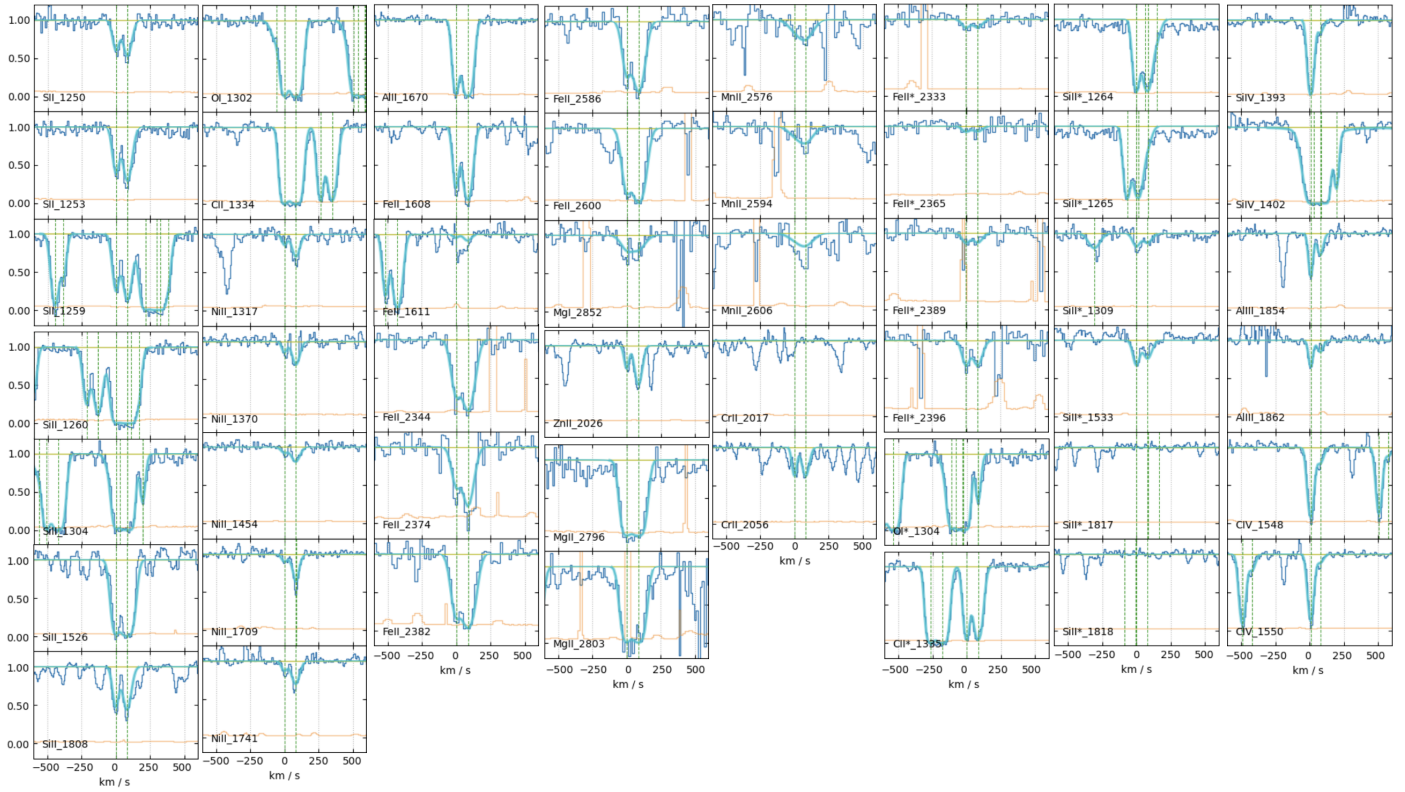


**Fig. A.1.** Set of Voigt profile fits for metal lines present in the spectrum of GRB 160203A *Best Data*, by combining single exposures RRM3, RRM4, and RRM5. The data are in blue, the fit is in cyan, the error spectrum is in orange, and the continuum level is in yellow. The vertical green dashed lines indicate the centre of the components.

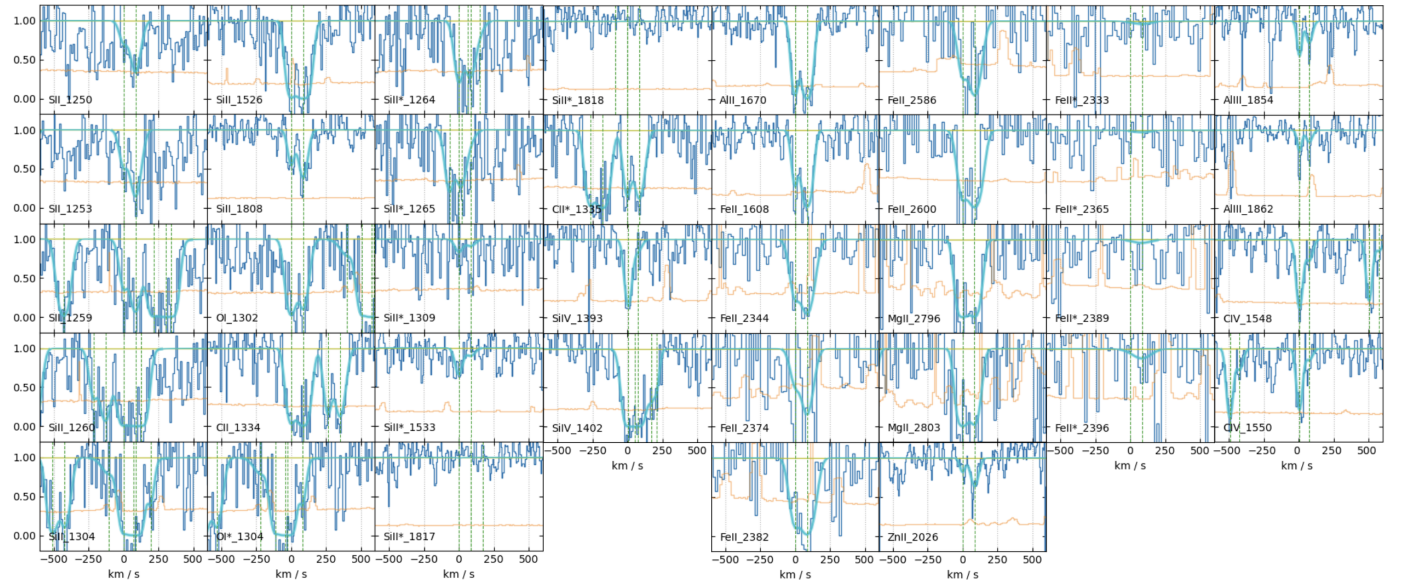


**Fig. A.2.** Set of Voigt profile fits for metal lines present in the spectrum of GRB 160203A Epoch 2. The data are in blue, the fit is in cyan, the error spectrum is in orange, and the continuum level is in yellow. The vertical green dashed lines indicate the centre of the components.

**Appendix B: Column densities of low- and high-ionisation absorption lines for each observation****Table B.1.** RRM2 strongest components' column densities

Absorption lines	$\log(N_I/\text{cm}^{-2})$	$\log(N_{II}/\text{cm}^{-2})$	$\log(N_{TOT}/\text{cm}^{-2})$
Al II $\lambda$ 1670	>13.3	>13.9	>14.0
C II $\lambda$ 1334	>15.4	>15.5	>15.8
C II* $\lambda$ 1335	>14.6	>14.8	>15.0
Fe II $\lambda$ 1608, $\lambda$ 1611, $\lambda$ 2344, $\lambda$ 2374, $\lambda$ 2382, $\lambda$ 2586, $\lambda$ 2600	>14.5	14.72 $\pm$ 0.15	>14.9
Fe II* $\lambda$ 2333, $\lambda$ 2365, $\lambda$ 2389, $\lambda$ 2396	13.5 $\pm$ 0.2	13.2 $\pm$ 0.2	13.68 $\pm$ 0.15
Mg II $\lambda$ 2796, $\lambda$ 2803	>16.0	>15.3	>16.04
O I $\lambda$ 1302	>15.2	>16.0	>16.0
S II $\lambda$ 1250, $\lambda$ 1253, $\lambda$ 1259	15.2 $\pm$ 0.2	15.4 $\pm$ 0.2	15.61 $\pm$ 0.14
Si II $\lambda$ 1260, $\lambda$ 1304, $\lambda$ 1527, $\lambda$ 1808	15.56 $\pm$ 0.10	15.76 $\pm$ 0.10	15.97 $\pm$ 0.07
Si II* $\lambda$ 1264, $\lambda$ 1265, $\lambda$ 1309, $\lambda$ 1533, $\lambda$ 1817, $\lambda$ 1818	13.61 $\pm$ 0.11	13.44 $\pm$ 0.10	13.83 $\pm$ 0.08
Zn II $\lambda$ 2026	12.83 $\pm$ 0.10	13.18 $\pm$ 0.10	13.35 $\pm$ 0.08
$b$ (km s <sup>-1</sup> )	24 $\pm$ 2	34 $\pm$ 2	
Al III $\lambda$ 1854, $\lambda$ 1862	13.15 $\pm$ 0.06	12.9 $\pm$ 0.2	13.29 $\pm$ 0.07
C IV $\lambda$ 1548, $\lambda$ 1550	>14.4	13.34 $\pm$ 0.19	>14.4
Si IV $\lambda$ 1393, $\lambda$ 1402	>14.1	13.02 $\pm$ 0.11	>14.1
$b$ (km s <sup>-1</sup> )	16 $\pm$ 2	25 $\pm$ 2	

**Notes.** Column densities of the two strongest components (second and third columns) and the corresponding total column densities of the low-ionisation (upper panel) and high-ionisation (bottom panel) absorption lines of the RRM2 observation.

**Table B.2.** RRM3 strongest components' column densities

Absorption lines	$\log(N_I/\text{cm}^{-2})$	$\log(N_{II}/\text{cm}^{-2})$	$\log(N_{TOT}/\text{cm}^{-2})$
Al II $\lambda$ 1670	>13.4	>13.9	>14.0
C II $\lambda$ 1334	>15.7	>15.4	>15.9
C II* $\lambda$ 1335	>14.7	>14.8	>15.0
Fe II $\lambda$ 1608, $\lambda$ 1611, $\lambda$ 2344, $\lambda$ 2374, $\lambda$ 2382, $\lambda$ 2586, $\lambda$ 2600	>14.6	14.98 $\pm$ 0.04	>15.1
Fe II* $\lambda$ 2333, $\lambda$ 2365, $\lambda$ 2389, $\lambda$ 2396	13.39 $\pm$ 0.11	13.29 $\pm$ 0.11	13.64 $\pm$ 0.08
Mg I $\lambda$ 2852	12.27 $\pm$ 0.15	12.31 $\pm$ 0.10	12.60 $\pm$ 0.09
Mg II $\lambda$ 2796, $\lambda$ 2803	>15.9	>14.8	>15.9
Ni II $\lambda$ 1317, $\lambda$ 1370, $\lambda$ 1454, $\lambda$ 1709, $\lambda$ 1741	13.28 $\pm$ 0.14	13.99 $\pm$ 0.07	14.06 $\pm$ 0.06
O I $\lambda$ 1302	>15.6	>15.9	>16.1
O I* $\lambda$ 1304		13.60 $\pm$ 0.15	13.60 $\pm$ 0.15
S II $\lambda$ 1250, $\lambda$ 1253, $\lambda$ 1259	15.17 $\pm$ 0.10	15.44 $\pm$ 0.06	15.63 $\pm$ 0.10
Si II $\lambda$ 1260, $\lambda$ 1304, $\lambda$ 1527, $\lambda$ 1808	15.74 $\pm$ 0.02	15.69 $\pm$ 0.02	16.02 $\pm$ 0.01
Si II* $\lambda$ 1264, $\lambda$ 1265, $\lambda$ 1309, $\lambda$ 1533, $\lambda$ 1817, $\lambda$ 1818	13.85 $\pm$ 0.10	13.65 $\pm$ 0.06	14.06 $\pm$ 0.06
Zn II $\lambda$ 2026	12.77 $\pm$ 0.05	13.21 $\pm$ 0.03	13.34 $\pm$ 0.06
$b$ (km s <sup>-1</sup> )	22 $\pm$ 2	32 $\pm$ 2	
Al III $\lambda$ 1854, $\lambda$ 1862	13.09 $\pm$ 0.02	12.94 $\pm$ 0.04	13.32 $\pm$ 0.04
C IV $\lambda$ 1548, $\lambda$ 1550	>14.7	13.37 $\pm$ 0.06	>14.8
Si IV $\lambda$ 1393, $\lambda$ 1402	>14.1	13.02 $\pm$ 0.11	>14.1
$b$ (km s <sup>-1</sup> )	16 $\pm$ 2	25 $\pm$ 2	

**Notes.** Column densities of the two strongest components (second and third columns) and the corresponding total column densities of the low-ionisation (upper panel) and high-ionisation (bottom panel) absorption lines of the RRM3 observation.

**Table B.3.** RRM4 strongest components' column densities

Absorption lines	$\log(N_I/\text{cm}^{-2})$	$\log(N_{II}/\text{cm}^{-2})$	$\log(N_{TOT}/\text{cm}^{-2})$
Al II $\lambda 1670$	>13.6	>13.8	>14.0
C II $\lambda 1334$	>16.0	>15.9	>16.2
C II* $\lambda 1335$	>14.7	>14.6	>15.0
Fe II $\lambda 1608, \lambda 1611, \lambda 2344, \lambda 2374, \lambda 2382, \lambda 2586, \lambda 2600$	>14.6	14.99 $\pm$ 0.03	>15.1
Fe II* $\lambda 2333, \lambda 2365, \lambda 2389, \lambda 2396$	13.20 $\pm$ 0.12	13.30 $\pm$ 0.10	13.56 $\pm$ 0.07
Mg I $\lambda 2852$	12.28 $\pm$ 0.12	12.29 $\pm$ 0.09	12.59 $\pm$ 0.08
Mg II $\lambda 2796, \lambda 2803$	>15.9	>14.6	>15.9
Ni II $\lambda 1317, \lambda 1370, \lambda 1454, \lambda 1709, \lambda 1741$	13.61 $\pm$ 0.11	13.95 $\pm$ 0.06	14.12 $\pm$ 0.05
O I $\lambda 1302$	>15.8	>15.9	>16.2
O I* $\lambda 1304$		13.44 $\pm$ 0.15	13.44 $\pm$ 0.15
S II $\lambda 1250, \lambda 1253, \lambda 1259$	15.20 $\pm$ 0.10	15.43 $\pm$ 0.06	15.63 $\pm$ 0.10
Si II $\lambda 1260, \lambda 1304, \lambda 1527, \lambda 1808$	15.70 $\pm$ 0.02	15.85 $\pm$ 0.02	16.08 $\pm$ 0.01
Si II* $\lambda 1264, \lambda 1265, \lambda 1309, \lambda 1533, \lambda 1817, \lambda 1818$	13.97 $\pm$ 0.10	13.69 $\pm$ 0.06	14.16 $\pm$ 0.07
Zn II $\lambda 2026$	12.72 $\pm$ 0.04	13.23 $\pm$ 0.02	13.35 $\pm$ 0.02
$b$ (km s <sup>-1</sup> )	21 $\pm$ 2	33 $\pm$ 2	
Al III $\lambda 1854, \lambda 1862$	13.11 $\pm$ 0.02	12.79 $\pm$ 0.04	13.28 $\pm$ 0.02
C IV $\lambda 1548, \lambda 1550$	>14.6	13.19 $\pm$ 0.07	>14.6
Si IV $\lambda 1393, \lambda 1402$	>14.4	12.60 $\pm$ 0.16	>14.4
$b$ (km s <sup>-1</sup> )	17 $\pm$ 2	23 $\pm$ 2	

**Notes.** Column densities of the two strongest components (second and third columns) and the corresponding total column densities of the low-ionisation (upper panel) and high-ionisation (bottom panel) absorption lines of the RRM4 observation.

**Table B.4.** RRM5 strongest components' column densities

Absorption lines	$\log(N_I/\text{cm}^{-2})$	$\log(N_{II}/\text{cm}^{-2})$	$\log(N_{TOT}/\text{cm}^{-2})$
Al II $\lambda 1670$	>13.6	>13.8	>14.0
C II $\lambda 1334$	>15.9	>15.5	>16.1
C II* $\lambda 1335$	>14.9	>14.8	>15.1
Fe II $\lambda 1608, \lambda 1611, \lambda 2344, \lambda 2374, \lambda 2382, \lambda 2586, \lambda 2600$	>14.6	15.00 $\pm$ 0.02	>15.1
Fe II* $\lambda 2333, \lambda 2365, \lambda 2389, \lambda 2396$	13.09 $\pm$ 0.19	13.27 $\pm$ 0.14	13.49 $\pm$ 0.11
Mg I $\lambda 2852$	12.18 $\pm$ 0.19	12.13 $\pm$ 0.16	12.46 $\pm$ 0.13
Mg II $\lambda 2796, \lambda 2803$	>16.0	>14.3	>16.0
Ni II $\lambda 1317, \lambda 1370, \lambda 1454, \lambda 1709, \lambda 1741$	13.39 $\pm$ 0.14	13.96 $\pm$ 0.06	14.06 $\pm$ 0.05
O I $\lambda 1302$	>15.9	>15.9	>16.2
O I* $\lambda 1304$		13.97 $\pm$ 0.19	13.97 $\pm$ 0.19
S II $\lambda 1250, \lambda 1253, \lambda 1259$	15.30 $\pm$ 0.10	15.45 $\pm$ 0.06	15.68 $\pm$ 0.10
Si II $\lambda 1260, \lambda 1304, \lambda 1527, \lambda 1808$	15.66 $\pm$ 0.02	15.84 $\pm$ 0.02	16.06 $\pm$ 0.01
Si II* $\lambda 1264, \lambda 1265, \lambda 1309, \lambda 1533, \lambda 1817, \lambda 1818$	13.90 $\pm$ 0.09	13.79 $\pm$ 0.05	14.15 $\pm$ 0.05
Zn II $\lambda 2026$	12.79 $\pm$ 0.03	13.23 $\pm$ 0.02	13.36 $\pm$ 0.02
$b$ (km s <sup>-1</sup> )	20 $\pm$ 2	34 $\pm$ 2	
Al III $\lambda 1854, \lambda 1862$	13.10 $\pm$ 0.02	12.66 $\pm$ 0.05	13.22 $\pm$ 0.02
C IV $\lambda 1548, \lambda 1550$	>14.6	13.31 $\pm$ 0.05	>14.6
Si IV $\lambda 1393, \lambda 1402$	>14.4	12.94 $\pm$ 0.07	>14.5
$b$ (km s <sup>-1</sup> )	17 $\pm$ 2	23 $\pm$ 2	

**Notes.** Column densities of the two strongest components (second and third columns) and the corresponding total column densities of the low-ionisation (upper panel) and high-ionisation (bottom panel) absorption lines of the RRM5 observation.

**Table B.5.** Epoch 2 strongest components' column densities

Absorption lines	$\log(N_I/\text{cm}^{-2})$	$\log(N_{II}/\text{cm}^{-2})$	$\log(N_{TOT}/\text{cm}^{-2})$
Al II $\lambda 1670$	>13.4	>13.7	>13.9
C II $\lambda 1334$	>15.4	>15.7	>15.9
C II* $\lambda 1335$	>14.6	>14.7	>15.0
Fe II $\lambda 1608, \lambda 1611, \lambda 2344, \lambda 2374, \lambda 2382, \lambda 2586, \lambda 2600$	>14.5	15.15 $\pm$ 0.12	>15.2
Fe II* $\lambda 2333, \lambda 2365, \lambda 2389, \lambda 2396$	13.2 $\pm$ 0.2	13.2 $\pm$ 0.5	13.5 $\pm$ 0.3
Mg II $\lambda 2796, \lambda 2803$	>16.1	>15.0	>16.1
O I $\lambda 1302$	>16.1	>15.1	>16.1
S II $\lambda 1250, \lambda 1253, \lambda 1259$	15.1 $\pm$ 0.2	15.7 $\pm$ 0.2	15.8 $\pm$ 0.2
Si II $\lambda 1260, \lambda 1304, \lambda 1527, \lambda 1808$	15.61 $\pm$ 0.12	15.86 $\pm$ 0.12	16.05 $\pm$ 0.11
Si II* $\lambda 1264, \lambda 1265, \lambda 1309, \lambda 1533, \lambda 1817, \lambda 1818$	13.66 $\pm$ 0.17	13.45 $\pm$ 0.15	13.87 $\pm$ 0.12
Zn II $\lambda 2026$	12.54 $\pm$ 0.18	13.06 $\pm$ 0.10	13.17 $\pm$ 0.10
$b$ (km s <sup>-1</sup> )	24 $\pm$ 2	35 $\pm$ 2	
Al III $\lambda 1854, \lambda 1862$	12.9 $\pm$ 0.2	12.8 $\pm$ 0.2	13.2 $\pm$ 0.2
C IV $\lambda 1548, \lambda 1550$	>14.4	>13.4	>14.5
Si IV $\lambda 1393, \lambda 1402$	>14.4	>12.7	>14.4
$b$ (km s <sup>-1</sup> )	17 $\pm$ 2	27 $\pm$ 2	

**Notes.** Column densities of the two strongest components (second and third columns) and the corresponding total column densities of the low-ionisation (upper panel) and high-ionisation (bottom panel) absorption lines of the Epoch 2 observation.